An Experimental Study and Database for Tip Vortex Flow From An Airfoil

K.B.M.Q. Zaman, Amy F. Fagan, and Mina R. Mankbadi
Glenn Research Center, Cleveland, Ohio

NASA STI Program . . . in Profile

Since its founding, NASA has been dedicated to the advancement of aeronautics and space science. The NASA Scientific and Technical Information (STI) Program plays a key part in helping NASA maintain this important role.

The NASA STI Program operates under the auspices of the Agency Chief Information Officer. It collects, organizes, provides for archiving, and disseminates NASA's STI. The NASA STI Program provides access to the NASA Technical Report Server—Registered (NTRS Reg) and NASA Technical Report Server—Public (NTRS) thus providing one of the largest collections of aeronautical and space science STI in the world. Results are published in both non-NASA channels and by NASA in the NASA STI Report Series, which includes the following report types:

- TECHNICAL PUBLICATION. Reports of completed research or a major significant phase of research that present the results of NASA programs and include extensive data or theoretical analysis. Includes compilations of significant scientific and technical data and information deemed to be of continuing reference value. NASA counter-part of peer-reviewed formal professional papers, but has less stringent limitations on manuscript length and extent of graphic presentations.

- TECHNICAL MEMORANDUM. Scientific and technical findings that are preliminary or of specialized interest, e.g., "quick-release" reports, working papers, and bibliographies that contain minimal annotation. Does not contain extensive analysis.

- CONTRACTOR REPORT. Scientific and technical findings by NASA-sponsored contractors and grantees.

- CONFERENCE PUBLICATION. Collected papers from scientific and technical conferences, symposia, seminars, or other meetings sponsored or co-sponsored by NASA.

- SPECIAL PUBLICATION. Scientific, technical, or historical information from NASA programs, projects, and missions, often concerned with subjects having substantial public interest.

- TECHNICAL TRANSLATION. English-language translations of foreign scientific and technical material pertinent to NASA's mission.

For more information about the NASA STI program, see the following:

- Access the NASA STI program home page at http://www.sti.nasa.gov

- E-mail your question to help@sti.nasa.gov

- Fax your question to the NASA STI Information Desk at 757-864-6500

- Telephone the NASA STI Information Desk at 757-864-9658

- Write to:
  NASA STI Program
  Mail Stop 148
  NASA Langley Research Center
  Hampton, VA 23681-2199

An Experimental Study and Database for Tip Vortex Flow From An Airfoil

K.B.M.Q. Zaman, Amy F. Fagan, and Mina R. Mankbadi
Glenn Research Center, Cleveland, Ohio

National Aeronautics and
Space Administration

Glenn Research Center
Cleveland, Ohio 44135

November 2017

Acknowledgments

Level of Review: This material has been technically reviewed by technical management.

An Experimental Study and Database for Tip Vortex Flow From an Airfoil

K.B.M.Q. Zaman, Amy F. Fagan, and Mina R. Mankbadi
National Aeronautics and Space Administration
Glenn Research Center
Cleveland, Ohio 44135

Summary

An experimental investigation of tip vortices from a NACA0012 airfoil is conducted in a low-speed wind tunnel at a chord Reynolds number (R_c) of 4×10^4. Data for the stationary airfoil at various angles of attack (α) are first discussed. Detailed flow-field surveys are done for two cases: $\alpha = 10°$ with attached flow and $\alpha = 25°$ with massive flow separation. Data include mean velocity, streamwise vorticity, and turbulent stresses at various streamwise locations. For all cases, the vortex core is seen to involve a mean velocity deficit. The deficits in these cases trace to the airfoil wake, part of which gets wrapped up by the tip vortex. Comparison with data from the literature suggests that with increasing R_c, the deficit turns into an excess, with the transition occurring in the approximate R_c range of 2×10^5 to 5×10^5. Survey results for various shapes of the airfoil wingtip are then presented. The shapes include square and rounded ends and a number of winglet designs. Finally, data under sinusoidal pitching condition, for the airfoil with square ends, are documented. All pitching cases pertain to a mean $\alpha = 15°$, while the amplitude and frequency are varied. Amplitudes of $\pm5°$, $\pm10°$, and $\pm15°$ and reduced frequencies $k = 0.08$, 0.2, and 0.33 are covered. Digital records of all data and some of the hardware design are made available on a supplemental CD with the electronic version of the paper for those interested in numerical simulation.

Introduction

Tip vortices pertain to a wide variety of applications. They are of concern in tip clearance losses in turbomachinery, noise from rotorcraft and submarine propellers, safety and efficiency in aircraft traffic control as well as performance of all lifting vehicles. A strong tip vortex may imply losses in performance and therefore a reduction in its strength may be sought through design considerations and flow control. There is a need for a deeper fundamental understanding of the associated fluid dynamics. Across various disciplines, designers stand to benefit from a better understanding of phenomena such as the formation and merger of vortex systems from the pressure and suction sides of a lifting surface, migration of velocity deficit and turbulence from the wake of the lifting body affecting subsequent behavior of the tip vortex, mean velocity deficit or excess within the vortex core, and the lifespan and stability characteristics of the vortex. Flow control efforts aiming to weaken tip vortex strength can also benefit from a better understanding of the flow dynamics.

Dreyer et al. (Ref. 1) qualitatively explored the effect of tip leakage vortices on cavitation erosion issues relevant to turbines. For low-speed flows, they incrementally decreased the gap size between the "runner" and the "discharge ring" until the vortex intensity reached a maximum followed by a sharp decrease. Tip clearance gap size, which dictated the tip vortex strength, was also identified to be a critical parameter in cooling strategies in high-pressure turbines (Ref. 2); a numerical study of flow and heat transfer in axial turbines is described in Reference 3. Casalino et al. (Ref. 4) studied tip vortex rollup and its impact on airframe noise. Their analysis revealed a connection between the far-field noise and the kinematics of the two vortices generated from the lower and upper edges of the wingtip. For an aircraft,

the tip vortex is responsible for induced drag and increased noise. It also dictates the safe distance needed between aircraft in air traffic control (Ref. 5). Various flow control studies have also been carried out in order to reduce the strength of the tip vortex (Refs. 2 and 6 to 8).

A body of fundamental studies on tip vortices from rectangular wing sections (static) exists in the literature (e.g., Refs. 9 to 16). A few of these are briefly reviewed here and data from some others will be compared later with the present results. A NACA0012 section (chord, $c = 0.203$ m) with square tip (not rounded) was used by Devenport et al. (Ref. 11). A four-sensor hot-wire probe was used to acquire the data at a chord Reynolds number (R_c) of 5.3×10^5. The downstream evolution of the flow was studied over $5 < x/c < 30$. (Cited x-locations are converted to current convention with origin located at one-quarter chord from the leading edge (LE). Also, all data in the following sections will be presented in nondimensional form as defined in the Experimental Procedure section.) Streamwise vorticity (ω_X) and turbulent spectra data were discussed. The issue of probe interference and spatial "wandering" of the vortex was addressed and both effects were inferred not to be significant within their measurement domain. Chow et al. (Ref. 12) made detailed measurements for a NACA0012 half-wing section with a rounded tip (1.22 m chord by 0.91 m span) at $R_c = 4.6 \times 10^6$. Data were acquired by a seven-hole pressure probe and a triple-wire hot-wire probe. The emphasis was around the tip region and the measurement domain extended downstream up to $x/c = 1.43$. Distributions of cross-flow velocity, $(V^2 + W^2)^{1/2}$, and streamwise velocity, U, were presented to study the initial formation of the tip vortex. Ramaprian and Zheng (Ref. 13) did similar measurements over the x/c range of 1.08 to 4.08, for $R_c = 1.8 \times 10^5$. They used laser Doppler velocimetry and provided U and ω_X data. Birch et al. (Ref. 15) carried out measurements with a NACA0015 and a cambered airfoil; both had square tips. Their measurements at $R_c = 2 \times 10^5$ were carried out by a seven-hole probe and distributions of U as well as ω_X were discussed.

Despite these research results and the progress achieved so far, many of the cited studies made an appeal for further fundamental studies of a tip vortex. In Reference 5, the outlook for prediction as related to air traffic control is summarized as "distinct improvements in our ability to predict the motion and persistence of trailing vortices are needed before analysis is widely of value." In connection with noise generation, authors of Reference 4 commented that "the role of turbulent fluctuations…and their ingestion by, and roll up into, the tip vortices needs to be investigated in more detail." Similar comments are made in Reference 17 in connection with tip vortex dynamics in wind turbines and rotorcrafts as well as in several of the other cited references. The present work is motivated by such calls. An experiment is carried out utilizing mostly existing hardware and facilities to study the tip vortex characteristics from a rectangular airfoil section. First, a parametric study is performed with the angle of attack (α) varied statically.

The shape of the airfoil tip is known to affect the tip vortex characteristics. This issue is addressed next. Besides square versus rounded tips, the effect of various winglet shapes is explored. These experiments are done for stationary airfoils with $\alpha = 10°$ and $\alpha = 25°$.

Finally, dynamic effects under periodically pitched conditions are explored. In many applications, especially with rotorcraft and turbomachinery, the effective α may vary within the rotation cycle. This is likely to affect the tip vortex dynamics. Such effects have been explored only in a few past experiments. For example, the authors of both References 13 and 15 followed up their studies of static airfoils with experiments where the airfoil was oscillated periodically in pitch (Refs. 18 and 19). In the present study, a mechanism existing from prior experiments is used to also explore the dynamic effects. The mechanism is capable of oscillating the airfoil with variable frequency and amplitude in pitch. Data are acquired with the airfoil oscillated about a mean α of 15°. As the results will show, the tip vortex undergoes transition to turbulence around this static α. Thus, this mean value of α was chosen with the thought that the dynamic effects might be pronounced around it.

The results of the entire study are documented in this report. After preliminary discussions, the static airfoil data are presented in the Static Airfoil Survey Results section. Some of these results were presented in a conference paper (Ref. 20). The data for different winglets are presented in the Effect of Tip Shape and Winglets section. Finally, the oscillating airfoil data are documented in the Oscillating Airfoil Results section. All data are also provided in digital format together with computer-aided-design (CAD) files for some of the hardware in order to aid numerical simulations should there be any interest.

Symbols

c	chord
f	frequency of oscillation, Hz
k	reduced frequency
R_c	chord Reynolds number
U	streamwise mean velocity
U_{core}	maximum or minimum mean velocity within vortex core
U_∞	tunnel velocity
u'	streamwise turbulence intensity
u'_{core}	maximum turbulence intensity within vortex core
V	transverse mean velocity
W	lateral mean velocity
x	streamwise coordinate
y	transverse coordinate
z	lateral coordinate
α	angle of attack
Γ	circulation
δ	winglet dihedral angle
ω_X	streamwise vorticity
v	kinematic viscosity

Experimental Procedure

The experiments are carried out in an open-loop, low-speed wind tunnel. The test section is 50 cm high by 76 cm wide and the 16:1 contraction ratio inlet has five flow conditioning screens. The flow is driven by an axial fan located on the downstream end. The airfoil used has a NACA0012 profile with 7.62 cm chord and 25.4 cm span; the model used for most of the data has a square tip with sharp edges. A picture of the wind tunnel test section is shown in Figure 1(a). The tunnel velocity, $U_\infty = 8$ m/s, corresponds to $R_c = 4 \times 10^4$. (Relative to many applications this R_c, dictated by facility constraints, is low; however, R_c may have only a minor influence at large α when flow separation occurs from near the LE. Furthermore, the low R_c flow may offer some advantage if the results are used for validation of unsteady numerical simulations.) The airfoil is supported from one wall while its other end stands free in the test section. A 0.635-cm-cylindrical rod attached to the airfoil passes through the wind tunnel wall and is supported outside by two bearings spaced 10 cm apart. The other end of the rod is attached to the oscillation (pitching) mechanism via a coupling (Figure 1(b) and Ref. 21). The data are first gathered for the airfoil held stationary at various α up to 35°. Detailed field properties are acquired for $\alpha = 10°$ and 25°.

Two crossed hot-wires, one in u-v and the other in u-w configuration and spaced 1.12 cm in z (Figure 1(c)), are used to obtain all three components of mean velocity and various turbulent stresses. The data from the u-w probe are appropriately shifted to coincide with grid points covered by the u-v probe.

Probe traversing mechanisms, with 0.025-mm resolution, are used under automated computer control. Gradients of the transverse mean velocities provide ω_X. For all data sets, the hot-wire calibration was checked at a fixed location in the freestream at the beginning and end of a run. The measured U values there were within 2 percent of tunnel velocity, U_∞. Those measured values of U from the two probes were later used to normalize the respective data from each probe for the given run. The value of U_∞ was monitored by a fixed Pitot-static probe along with each data point during the surveys. Root-mean-square deviation of U_∞ (with respect to the mean) was within 0.25 percent for all data sets presented. Uncertainty in the data is further discussed in the Results section. A standard personal computer (PC)-based National Instruments data system was used for data acquisition. Most of the data are based on 5 s averaging. Typical surveys on a cross-sectional plane at a fixed x location took about an hour.

Figure 1(c) shows the airfoil inside the test section with the two hot-wire probes located downstream. Figure 1(d) shows a schematic of the airfoil. The coordinate origin is located at the tip of the airfoil and at the support axis at one-quarter chord from the LE; positive-z ("inboard") direction is into the page. The airfoil is pitched about the z-axis. All oscillation case data are acquired with a mean $\alpha = 15°$ while varying the reduced frequency (k) and the amplitude of oscillation. The oscillation is sinusoidal in pitch. The oscillation cases are denoted as $15°\pm\Delta\alpha$ where $\Delta\alpha$ is the swing amplitude in degrees. The two measurement planes marked "A" and "B" in Figure 1(d) will be explained later with the results.

> All distances are nondimensionalized by the chord ($c = 7.62$ cm), velocities by U_∞, and streamwise vorticity (ω_X) and circulation (Γ) by U_∞/c. The frequency of oscillation (f, Hz) is nondimensionalized as $k = \pi f c/U_\infty$.

In another set of experiments, a shorter-span airfoil model was used having the same NACA0012 shape. It had two locator pins at the end to which short attachments of same cross-sectional shape but with various tip shapes (winglets) could be attached. The total span of the airfoil with the attachments was the same as the original model. The attachments were fabricated by three-dimensional printing. Altogether, seven tip geometries were explored and one of them had a square shape to replicate the original model in order to check out data repeatability. The various attachments (winglets) are shown in Figure 2. CAD files for each of these designs are also included with this report.

Flow visualization was accomplished by introducing a tube of smoke (approximately 15 cm in diameter) from near the inlet of the tunnel and passed over the tip of the airfoil. The flow field was illuminated by a laser sheet. In another set of runs, global lighting was used in addition to the laser sheet in order to obtain a global view of the flow field associated with the tip vortex. (It is instructive to note that the smoke had to be cool with an approximate temperature the same as that of ambient. Initially, a generator was used that produced warm smoke with a temperature of about 50 °C. It resulted in a spurious "mushroom-" shaped vortical structure induced by buoyancy effects that was accentuated by the wind tunnel's contraction section. This completely obscured the tip vortex from the airfoil; see Figure A.1 in Appendix A.)

Results

Measurement Grid Sensitivity, Data Uncertainty, and Wandering of Vortex Core

Figure 3 shows flow visualization pictures of the tip vortex obtained by a laser sheet passing perpendicular to the flow at approximately $x = 3.2$ (recall that from here on all parameters are nondimensional). The airfoil is held fixed at various α and the view is from upstream at an angle to the x-axis (the camera and a small laser with optics in front, all located outside of the test section, can be seen

in Figure 1(a)). The tip vortex with clockwise rotation is evident at all values of α. The vortex is laminar at small α, but in the range of 15° to 20° it appears to transition to turbulence. Also with increasing α, at first it appears to gain strength, becoming the strongest around 10°, but gets diffused after transition at larger values of α. At $\alpha = 35°$, it is barely identifiable from the flow visualization pictures.

Detailed hot-wire surveys were conducted for various α at $x = 3.2$ and for limited α at various x. First, the results of a study on measurement grid sensitivity (spatial resolution) are discussed. Figure 4(a) shows contours of mean streamwise velocity (U) and ω_X for $\alpha = 25°$ while the grid size (same in y and z) was varied. The measurement domain was chosen after preliminary surveys to capture the core of the vortex. A mean velocity deficit occurs in the core. As expected, the magnitude of the velocity deficit (i.e., U-minimum within the vortex core, denoted in the following as U_{core}) and the peak in streamwise vorticity (denoted in the following as ω_X-peak) become less accentuated with increasing grid size. This is shown in the graph in Figure 4(b) from a set of similar measurements. The range in the legends of Figure 4(a) were chosen to show the distributions clearly; U_{core} and ω_X-peak values often exceeded the extrema in the legends. It can be seen that with decreasing grid size the amplitudes of U_{core} and ω_X-peak level out. Thus, for the case under consideration, a minimum grid size of about 0.05 was considered necessary.

With a very small grid size, a peculiarity was noted in data convergence. There was a lack of repeatability, especially in the ω_X data. Figure 5 shows ω_X measured with a coarse grid (0.073) in (a) and with a fine grid (0.018) in (b). With the coarse grid, the contours are relatively smooth and the vortex appears well defined from the ω_X contours. With the fine grid, the ω_X data in the core of the vortex has scatter. This is further examined in Figure 6, where ω_X measured in the core with different averaging times is shown, illustrating the scatter and lack of repeatability. The corresponding mean velocity distributions shown in Figure 7, overall, do not appear to have as much scatter. However, the velocity at a given point within the core varies quite a bit from plot to plot. The issue is further examined in Figure 8. For a given sampling record length, the data were acquired 12 times at a fixed point within the vortex core. This was repeated with record lengths varied from 1 to 256 s. Better convergence is achieved with increasing record length, as expected. However, even with 256 s averaging, there is still significant scatter.

Thus, while the overall vortex structure and its outer extents turn out well defined with just 5 s averaging (Figure 5(a)), there must be very low frequency fluctuations within the core of the vortex. Those fluctuations make the core ill defined when measured with smaller averaging times. In detailed surveys, it is not practical to use a long averaging time with the "point measurement" technique as with the hot-wires. For the 50 s averaging per point, as is the case at the lower right corner of Figure 6, the survey took about 3.5 h. (In spite of these and other limitations, the hot-wire technique was adopted for this study. Alternate "global measurement" techniques such as particle image velocimetry can have their own issues. For example, see the comment in parentheses at the end of the Experimental Procedure section and Appendix A indicating large sensitivity of the flow under consideration to buoyancy effects from seed particles.)

The scatter problem is further examined in Figure 9. Profiles of U and V were obtained using only the u-v probe. At each z-location, 100 s of data were recorded with a sampling rate of 200 Hz. The red profiles (line) are obtained by using all the data. The data records were then divided into 20 segments—each segment containing 5 s of data. For each z-location, the 20 data points from those segments are plotted with the square symbols. Within the core of the vortex (region of minimum U and maximum slope in V), there is large scatter when using 5 s averaging. However, away from the core, the scatter is much less. This also indicates that the outer extents of the tip vortex are relatively steady and explains why a well-defined vortex is measured when using coarser grids and covering a wider extent of the vortex cross

section. Many previous studies reported a meandering or wandering of the vortex at a slow rate. Reference 22 (and the Ph.D. dissertation of its first author) reported velocity fluctuations that had an organized component resulting in a low-frequency spectral peak (0.3 to 0.9 Hz). A low-frequency fluctuation underlying the turbulent signal in tip vortex flows can also be seen in the time trace data given in References 23 and 24. Reference 25 reported the wandering of the vortex core by several core diameters. However, other studies (e.g., Refs. 11 and 24) reported wandering in the amount of only a small fraction of the core radius. The present results indicate a low-frequency fluctuation within the very core of the vortex rather than any significant wandering of the overall vortex structure.

Grid sensitivity data as presented in Figure 4, but for $\alpha = 10°$ at $x = 3.2$, are shown in Figure 10. For this case, the flow over the airfoil is attached (see further discussion shortly), and thus the tip vortex is tighter in radius; note the difference in scale between Figure 4(a) and Figure 10(a). Thus, the 10° case required finer spatial resolution in the measurements. The data in Figure 10(b) suggest that a grid size of at least 0.015 may be required to resolve the flow. This is about the same as the probe volume (spacing of the sensors in a given X-probe) and thus represents the best that can be done with the X-wire technique. Once again with small grids, the time for the survey becomes prohibitively large. The data scatter for $\alpha = 10°$, as presented for $\alpha = 25°$ in Figure 9, is shown in Figure 11.

Therefore, the following was done for the results presented in this report.

> Data for the contour plots covering the full domain were acquired with coarse grids; thus, the peak levels within the vortex core in those plots are underestimates. However, the distributions outside the core are well represented. For properties in the cores (shown by line plots in later figures), separate runs were made with the finest grid size as necessary.

The full-field contour plots were used as guides to home in on the core for the latter surveys. Furthermore, most data in the report pertain to $x = 3.2$ and farther upstream one might need even better resolution. However, data from the literature (e.g., Ref. 12 and Figure 5(b) of Ref. 15) and the current data suggest that the vortex core size does not change significantly within the streamwise distance as covered in the present experiment. Also, at $\alpha = 25°$, there is massive flow separation and the wake is large; thus, the spatial resolution requirement is not as stringent. However, close to the airfoil trailing edge (TE) (e.g., at $x = 0.8$) there are hot-wire errors due to large turbulence. The contour plots are shown nonetheless to provide an idea about the overall extent of the shear layers. Actual magnitudes of U (blue inner regions in the contours) are likely to be lower and the corresponding plots should be considered qualitative.

A further discussion of the uncertainty in the data is pertinent. While it is difficult to specify the uncertainties pertaining to full survey domains at all x-locations, those for the core properties (shown by the line plots in later figures) were examined. First, simple cosine laws were used for data reduction from the X-wires. However, a prior yaw calibration check in the same facility showed significant errors only when the flow angle exceeded 20° from the streamwise direction (Ref. 26). The flow angularity even in the worst of the presented cases (see V and W data in the following section) are much smaller and thus, such errors may be considered small. A polynomial fit (through five adjacent data points) has been used to calculate the gradients of V and W for obtaining ω_X. This resulted in a smoothing and an underestimation of ω_X-peak values by about 2 percent in the $\alpha = 25°$ case and by about 10 percent in the $\alpha = 10°$ case (at $x = 3.2$). For each of the latter two α cases at $x = 3.2$, seven sets of data were examined for repeatability. These data sets were acquired over a span of several weeks. Grid sizes of 0.018 to 0.021 for $\alpha = 10°$ and 0.029 to 0.037 for $\alpha = 25°$ were considered. The repeatability for U_{core} was found to be

within ±2 percent of the respective mean value for either α case. For ω_X-peaks, on the contrary, it was found to be within ±7 percent and ±10 percent for the $\alpha = 25°$ and $\alpha = 10°$ cases, respectively.

Static Airfoil Survey Results

At low Reynolds numbers, the flow over the suction surface may undergo laminar separation even at small α. For $\alpha = 10°$ this was investigated by acquiring velocity profiles just downstream of the airfoil's TE. These measurements were done away from the tip ($z = 1.0$) and are expected to represent the state of the two-dimensional flow over most of the airfoil span. The data, shown in Figure 12, indicate that there is massive laminar separation at $U_\infty = 4.45$ m/s, indicated by the wide wake. With increasing velocity, the wake starts shrinking around $U_\infty = 6$ m/s, and beyond $U_\infty = 7.4$ m/s, further increases in U_∞ make only small changes. Thus, at the operating speed of $U_\infty = 8.0$ m/s, the flow on the upper surface is expected to be attached and free of significant laminar separation.

The y-profiles at $z = 1.0$ were acquired at several x stations downstream of the TE. The distributions of U, u', and V are shown in Figure 13(a) as contour plots for $\alpha = 10°$. It can be seen that the wake is narrow; the center of the wake shifts from $y = -0.135$ to -0.195 over the x-range covered. Turbulence intensity is high just downstream of the TE ($x = 0.8$) but decreases by the end of the x-range. The transverse velocity (V) is relatively small and it is negative in most of the domain. Corresponding data for $\alpha = 25°$ are shown in Figure 13(b). There is massive flow separation here and the wake is much wider. Turbulence intensity is very high on the lower part of the wake (negative y). The V component has large positive and negative values on the lower and the upper parts of the wake, respectively.

A motivation for the present experiment was to provide a dataset for validation of possible numerical simulation efforts. To that end, in order to provide a description of the flow field in the initial region, a few surveys were conducted around the tip of the airfoil. Figure 14 shows distributions of U, u', and V, on a vertical (x-y) plane and to the side of the airfoil tip (plane B in the schematic of Figure 1(d)). The measurement plane is at $z = -0.08$ and the data are shown in Figure 14(a) and (b) for $\alpha = 10°$ and $25°$, respectively. Due to the configuration of the probes (see the Experimental Procedure section), only the u-v probe could be brought close to the airfoil tip and the W component could not be acquired at the same plane. (The u-w probe was separated from u-v probe by 0.147 c. This is also why the z-extent of the measurement domain for quantities like W and ω_X, coincident with the u-v probe domain, is shorter.) The turbulence is low for $\alpha = 10°$, while it is large for $\alpha = 25°$. The V component is mostly positive (directed upward) at the measurement plane for both α cases.

Figure 15 shows data taken on a horizontal (x-z) plane just over the airfoil LE (plane A in the schematic of Figure 1(d)). Data for $\alpha = 10°$ taken at $y = 0.12$ are shown in Figure 15(a). Apart from U and u', both orthogonal mean velocity components (V and W) are also shown. In the measurement plane, for the attached flow with $\alpha = 10°$, turbulence is low. Upstream over the airfoil (negative x), the flow is marked by positive V but downstream it is negative. The W component is positive, consistent with the expected motion of the flow; fluid from below wraps around the tip of the airfoil and moves inboard on the upper surface. Similar patterns are also noted for $\alpha = 25°$ in Figure 15(b), except that the turbulence is high in the measurement plane. The survey plane for the latter case is somewhat higher ($y = 0.15$) in order to clear the upper reaches of the LE.

Detailed cross-sectional distributions of various properties at downstream locations are shown next. Only U, u', and ω_X data are discussed. Data at $x = 3.2$ are shown in Figure 16 for five values of α. Distributions of the three properties are shown in the three rows, as indicated in the caption. All three identify the location of the tip vortex. It is represented most unambiguously by the distribution of ω_X. An

inspection of the legends of the ω_X data indicate that vorticity in the core attains maximum amplitude in the α-range of 10° to 15° (recall that the peak levels in the contour plots are underestimates and representative values are discussed shortly). Comparison with the u' data shows that the vortex core is characterized by high turbulence intensity. The intensity jumps up significantly from $\alpha = 15°$ to 20°, indicating transition to a turbulent state. Comparison of U and ω_X data shows that the core of the vortex is associated with a velocity deficit at all values of α. Thus, the tip vortex core is seen to involve a "wake-like" profile in the present case. At smaller α, there are regions of excess velocity at upper and lower edges of the vortex core. These trends are discussed further in the following.

The vortex core region was surveyed with fine probe resolution. Based on such measurements, ω_X-peak and U_{core} values are shown in Figure 17(a) as a function of α. It can be seen that ω_X-peak at first increases with increasing α, reaches a maximum around $\alpha = 10°$, stays about the same for a range, and then abruptly drops around 16°. The initial increase in ω_X-peak is expected as lift increases with α. The tip vortex strength follows lift produced by the airfoil. It is not clear why ω_X-peak exhibits a plateau in the α-range of about 8° to 16°. Laminar separation or separation bubbles can produce peculiarities in the lift curve at low R_c (see, e.g., Refs. 27 and 28). It was discussed before (Figure 12) that massive laminar separation is unlikely in the present case. However, while circulation (Γ) may be directly proportional to lift coefficient, ω_X-peak may not follow the same trend. For the same amount of Γ, a vortex may be diffused over a larger area when ω_X-peak would be lower. The dropoff in ω_X-peak around 16° (Figure 17) is likely to be due to the onset of stall with a sudden decrease in lift; this is also tied to transition of the vortex core to a turbulent state. The value of U_{core} exhibits an initial drop then stays about the same (0.7 to 0.8) until dropping off around $\alpha = 16°$. The velocity deficit in the core attains as low a value as $U_{core} = 0.37$ just after stall, but then increases somewhat with a further increase in α. Peak turbulence intensity in the vicinity of the vortex core is shown separately in Figure 17(b). The most conspicuous feature is the rapid rise in the intensity around $\alpha = 16°$. The level reaches a maximum of $0.22 U_\infty$, but then gradually drops off with further increase in α.

The value of ω_X-peak of about 23 at $\alpha = 10°$ (Figure 17(a)) compares reasonably well with that (about 26) reported in Reference 15 for a NACA0015 wing at the same incidence (their Figure 5(d)). Comparable values were also reported in Reference 13 for a NACA0015 airfoil at $\alpha = 10°$ (their Figure 3). Similar data presented in Reference 11 (their Figure 8(c)) appears to indicate a much lower value for ω_X-peak. While detailed surveys were conducted in the work of Reference 12, unfortunately, ω_X data were not presented. It is interesting that in Reference 15, a significantly higher ω_X-peak value (about 40) was reported with a different (cambered) airfoil. These comparisons suggest that the peak vorticity may be sensitive to detailed geometry of the airfoil tip and its overall lift characteristics. Similar comparisons of the velocity deficit in the core (U_{core}) are discussed in the following paragraphs.

The streamwise evolution of the flow field for $\alpha = 10°$ is presented in Figure 18. U, u', and ω_X data are shown similarly as in Figure 16, for five x-stations. As noted before, comparison of U- and ω_X-distributions shows that there are regions of high U both above and below the vortex core at all stations. However, the core location is marked by a region of low U. At the upstream-most location, it can be seen that the velocity deficit in the core is connected with the region of velocity defect from the wake of the airfoil (the latter is seen as the band of horizontal contours in blue). Further downstream, the vortex core moves to the right (inboard) while the wake of the airfoil recedes farther inboard. The turbulence intensity in the core is relatively high at locations close to the airfoil ($x = 0.8$), but has diminished substantially farther downstream. The high intensity up close to the TE also appears to be due to ingestion of airfoil wake fluid into the core of the tip vortex. In order to assist possible numerical simulations, the V and W

components of the velocity corresponding to the data of Figure 18 are documented in Appendix B; the turbulent stresses are given in Appendix C.

Similar data for $\alpha = 25°$ are shown in Figure 19. At $x = 0.8$, the vortex appears ill-defined. However, by $x = 1.6$, the tip vortex has taken clear shape. At this α, peak vorticity is much smaller while turbulence intensity is much larger, relative to the $\alpha = 10°$ case. Overall, the ω_X distribution has an oblong shape that gently rotates clockwise with increasing downstream distance. The U-distribution exhibits a similar overall trend as described for the $\alpha = 10°$ case. From the two sets of data shown in Figure 18 and Figure 19, it is apparent that the velocity deficit region within the vortex core has its origin in the wake from the airfoil. Part of the wake is pulled off and gets wrapped into the vortex core. The deficit persists at the farthest downstream location covered in the experiment. As with the $\alpha = 10°$ case, other flow properties for the $\alpha = 25°$ case are given in Appendixes D and E.

The variations of ω_X-peak and U_{core} with x for $\alpha = 10°$ and $25°$ are shown in Figure 20(a) and (b), respectively, in a similar manner as in Figure 17(a). For $\alpha = 10°$, ω_X-peak initially increases, reaching a maximum around $x = 1.75$, and then decreases with farther increase in x (Figure 20(a)). This trend is somewhat different from that reported in Reference 15 where the level practically remained a constant over the x-range covered (see earlier discussion of Figure 17). The trend of U_{core} is not well defined, but it generally follows that of the ω_X-peak. At $\alpha = 25°$ (Figure 20(b)), on the contrary, a clear trend has emerged for U_{core}. As the separated flow from the wake of the airfoil is ingested within the vortex, U_{core} is very low initially. Farther downstream it increases and levels off at a value of about 0.6. The amplitude of ω_X-peak for this case is seen to be roughly five times lower compared to that for the $\alpha = 10°$ case, and stays within the range of 4.5 to 5.5.

The axial flow (U-distribution) within the tip vortex has a "rich behavior;" quoting from Reference 5 in connection with review of airplane wingtip vortex data, "it has surprised many of us that the velocity relative to the atmosphere may be directed towards the airplane but also away from it." For $\alpha = 10°$, Chow et al. (Ref. 12) reported a large excess velocity, up to 1.77 U_∞; (if extrapolated to $x = 3$, the value is about 1.5 U_∞). On the contrary, a velocity deficit is reported in Reference 13 (0.68 to 0.78 U_∞, their Figure 2). In Reference 15, a velocity excess is reported for the cambered airfoil (1.1 to 1.3 U_∞), but just about 1.0 U_∞ for the NACA0015 airfoil (their Figure 5(e)). A velocity deficit is also reported in Reference 11 (their Figure 20). Approximate values of U_{core} observed in some previous experiments are listed in Table I. It appears to be an issue researchers have hardly agreed on. Clearly, the airfoil geometry and operating conditions must play a role. From data at various α, it has been reasoned in previous studies (Ref. 14) that U_{core} might be correlated with the net Γ around the tip vortex. From Table I, pertinent to $\alpha \approx 10°$ and symmetric airfoils such as NACA0012 and NACA0015, there also appears to be a Reynolds number dependence. Approximately $2 \times 10^5 < R_c < 5 \times 10^5$ is a range above which a jet-like behavior is noted, whereas below that range a wake-like behavior is consistently observed. The phenomenon and its reason, however, remain far from conclusive. In the present case at the low R_c, the core is always seen to involve a velocity deficit. Tracing the evolution of the core, it is also apparent that the deficit has its origin in the wake from the airfoil. Part of the wake is ingested by the tip vortex that manifests as the deficit. After an initial increase in magnitude, it persists practically unabated as far downstream as is covered in the experiment.

The excess velocities ($U > 1$) seen above and below the vortex core for the $\alpha = 10°$ case (Figure 18) also seem to have their origin in the flow near the LE. Past the stagnation point, the flow accelerates as it passes over the LE of the airfoil. Thus, there is a region over the LE where $U > 1$ (a classic example is the occurrence of shocks over an airplane wing during subsonic flight). Similarly, there is also a region of excess U underneath the LE even though its magnitude is not as high as seen over the LE. It is apparent

TABLE I.—APPROXIMATE VALUE OF MAXIMUM OR MINIMUM
MEAN VELOCITY WITHIN TIP VORTEX (U_{core}) FROM
VARIOUS EXPERIMENTS AT OR ABOUT $\alpha = 10°$

Reference	R_c 1×10^{-5}	U_{core}
Chow et al. 1997 (Ref. 12)	46.0	1.77
McAlister and Takahashi 1991 (Ref. 29)	15.0	1.25
Anderson and Lawton 2003, rounded tip (Ref. 14)	12.5	1.37
Anderson and Lawton 2003, square tip (Ref. 14)	12.5	1.12
Chigier and Corsiglia 1971 (Ref. 25)	9.5	1.15
Orloff 1974 (Ref. 10)	7.0	1.05
Devenport et al. 1996 (Ref. 11)	5.30	0.86
Lee and Pereira 2010 (Ref. 16)	3.0	0.88
Corsiglia et al. 1973 (Ref. 9)	3.0	0.80
Birch et al. 2004 (Ref. 15)	2.0	1.00
Ramaprian and Zheng 1997 (Ref. 13)	1.8	0.78
Present, square tip	0.4	0.78
Present, rounded tip	0.4	0.79

that these high velocity regions persist downstream and manifest as the regions of excess U above and below the tip vortex core. A similar effect also occurs at $\alpha = 25°$, however, the flow acceleration around the LE is diminished due to massive separation. Regions of higher velocities can indeed be detected in Figure 19, especially above the tip vortex, even though the magnitudes are barely above unity.

The trajectories of the vortex core, as determined from ω_X-peak location, for $\alpha = 10°$ and 25° are documented in Figure 21. The core location data on x-z and x-y planes are shown in Figure 21(a) and (b), respectively. The movement of the core for $\alpha = 25°$ is more pronounced. With increasing x, the core moves inboard (positive z) and downward (negative y). A similar movement is also noted for $\alpha = 10°$, albeit the magnitudes are smaller. Similar data could be found in Reference 13. At $\alpha = 10°$ and with increasing x, an inboard movement of the core in z was reported. However, there was a clear "rise" in y (their Figure 5); the magnitudes were also relatively large compared to the present $\alpha = 10°$ data. The reasons for the different behavior in the y-direction remain unclear but are likely due to differences in geometric and operating conditions.

Effect of Tip Shape and Winglets

Flow-field surveys were conducted for all tip shape cases shown in Figure 2. The winglet dihedral angle, δ, may be defined as the angle between the planes of the winglet and the wing (airfoil) itself. Thus, the "winglet-up" and "winglet-down" cases of Figure 2(b) and (c) are denoted by $\delta = +90°$ and $\delta = -90°$, respectively. The surveys were done for two fixed angles of attack, $\alpha = 10°$ and $\alpha = 25°$. For $\alpha = 10°$, the results are shown in Figure 22 to Figure 25. The cases include square versus rounded tip in Figure 22, winglet-up versus winglet-down cases in Figure 23, winglet-up (repeated) and triangular winglet cases in Figure 24, and angled-out ($\delta = 45°$) and angled-in ($\delta = 135°$) cases in Figure 25. Little difference is noted between the square- and the rounded-tip cases (Figure 22). The velocity deficit (U_{core}) turns out basically the same. Square- versus round-tip shape was also found to have little impact on the transverse velocity

profiles in Reference 14 for $\alpha = 10°$, at $x = 2$ and $R_c \approx 10^6$ (their Figure 6); although significant differences occurred at lower values of α. On the contrary, referring back to Table I, a large difference in the core velocity was reported in that reference at $R_c = 1.25 \times 10^6$. The velocity excess (U_{core}) increased from 1.15 for the square case to 1.37 with the rounded case (their Figure 4). The flow visualization results of Reference 22 also showed a large difference in the initial rollup of the tip vortex between these two tip shapes. Reference 7 reported differences in the response of the tip vortex to flow control efforts when using the two different tip shapes. The overall lack of sensitivity of the tip shape observed in the present experiment might be characteristic of low R_c flows. However, this remains inconclusive. A close inspection of the present data does indicate some differences; for example, the peak vorticity level and the peak turbulence are found to be somewhat higher for the rounded-tip case.

Referring back to the Measurement Grid Sensitivity, Data Uncertainty, and Wandering of Vortex Core section, note that the data in Figure 22 to Figure 25 are obtained from coarse grid measurements, and thus, the "ω_X-peak" values are underestimates (and hence the quotes). Values for "ω_X-peak" are found to be 16.6 and 20.5 for the square- and rounded-tip cases, respectively. These values are tabulated in Table II for the two tip shapes and all winglet cases (for which field data are discussed shortly) for comparison purposes. (Recall from earlier discussion that the actual value of ω_X-peak for the square tip is about 23 as opposed to 16.4 listed in Table II.) Anyway, the rounded tip appears to result in a more concentrated vorticity and hence a higher "ω_X-peak" value. However, estimates of the Γ (obtained by integrating ω_X over the measurement domain) are found to be practically the same. The Γ parameter, which should be largely independent of the measurement grid density, is also listed in Table II.

Corresponding data shown in Figure 23 for the winglet-up and winglet-down cases exhibit significant effects. As can be seen from these plots and the data in Table II, peak vorticity values are lower compared to the cases in Figure 22. The winglets have weakened the tip vortex. Also, the winglet-down case has resulted in a splitting of the tip vortex. Similar observations were reported by Gerontakos and Lee (Ref. 30) in experiments with a "winglet dihedral" together with a swept wing section. They observed two vortical structures and inferred that one of them originated from the junction of the wing and the dihedral (junction vortex (JV)) while the other one was the TV. It is possible that a similar phenomenon occurs with the winglet-down case—the vortex with center around $y = z = 0$ is the JV whereas the other one is the TV. It is not clear, however, why such a dual vortical structure did not occur in the present winglet-up case. The large differences in the geometries between the present work and Reference 30 might have caused the different behavior; the work in Reference 30 involved a swept and tapered wing as opposed to a rectangular wing in the present work.

TABLE II.—COMPARATIVE VALUES OF PEAK VORTICITY ("ω_X-peak") AND CIRCULATION (Γ) FOR DIFFERENT TIP SHAPE (WINGLET) CASES, OBTAINED FROM THE COARSE GRID MEASUREMENT DATA OF FIGURE 22 TO FIGURE 29

Tip shape	$\alpha = 10°$		$\alpha = 25°$	
	"ω_X-peak"	Γ	"ω_X-peak"	Γ
Straight square	16.64	191.9	4.41	85.6
Straight rounded	20.45	196.0	3.95	81.6
Winglet up	14.34	198.0	2.48	83.7
Winglet down	12.26	196.6	2.41	86.0
Triangular	10.1	207.7	3.31	82.4
Angled out	16.3	210.7	3.13	68.3
Angled in	10.7	206.4	4.07	93.1

The value of "ω_X-peak" is seen to drop the most for the triangular (Figure 24) and the angled-in (Figure 25) cases. For the angled-in case, the mean velocity deficit (U_{core}) is also found to be the most pronounced among all cases studied. $U_{core} = 0.72$ is noted from Figure 25; recall, once again, these are coarse grid data and the actual U_{core} value is likely to be even less. (For comparison, for the rounded-tip case in Figure 22, U_{core} is found to be 0.85, whereas fine grid measurements yielded a value of 0.79, Table I). Once again, even though "ω_X-peak" value has decreased with the winglets, the Γ value has remained approximately the same (Table II). Although the Γ produced did not change, the tightness of the vortex core and peak vorticity was affected significantly by the tip shapes. In Table II, for $\alpha = 10°$, the variation in Γ is within 8.9 percent, whereas the variation in "ω_X-peak" is as much as 48 percent.

Similar data for different tip shape cases for $\alpha = 25°$ are shown in Figure 26 to Figure 29. For these stalled flows, the tip vortex is spread over a larger cross-sectional area. Again, there is little difference between the square- and the rounded-tip cases (Figure 26). The winglet-down case (Figure 27) shows a split vortex as seen with $\alpha = 10°$. The values of Γ and "ω_X-peak" for the different cases are listed in Table II. Since the measurement domain has not captured the full extent of the tip vortex in some cases (e.g., for the winglet-down case in Figure 27), estimates of Γ are not as good as with the $\alpha = 10°$ cases. Here, variation in Γ is found to be within 26 percent, whereas the variation in "ω_X-peak" is within 45 percent.

Oscillating Airfoil Results

Data were acquired with the airfoil pitched sinusoidally about the *z*-axis with a mean $\alpha = 15°$. Nondimensional oscillation frequencies ($k = \pi f c / U_\infty$) of 0.08, 0.2, and 0.33 were covered. Dynamic stall from a two-dimensional flow (airfoil spanning the entire width of the test section) was studied before for comparable range of *k* in the same facility (Ref. 21). The highest *k* with the given U_∞ (8 m/s) corresponded to a physical frequency of 10.2 Hz. This was the limit beyond which structural issues might become a concern. Amplitudes of $\pm 2.5°$, $\pm 5°$, $\pm 10°$, and $\pm 15°$ were covered.

Figure 30 shows flow visualization pictures from a movie sequence for oscillation at $k = 0.2$ (6.5 Hz, $\alpha = 15° \pm 10°$). The pictures correspond to certain values of α as indicated, the arrows denoting the direction of motion. The upward arrow denotes pitch-up motion, that is, α decreasing and vice versa. The frames are chosen such that there are pairs at approximately the same α, but with the opposite direction of motion. The framing rate was 500/s and the laser-sheet location is at $x = 3.2$. Additional floodlighting is used in order to obtain a global view. The pitching motion of the airfoil with varying frames can be seen and the laser-sheet illuminated cross section bears resemblance to the stationary airfoil data shown in Figure 2. Comparison of the pictures at the same α, but with a different direction of motion, reveals that the tip vortex is somewhat more organized during the pitch-up motion (α decreasing) compared to the pitch-down (α increasing) motion. This is discussed further in the following paragraphs.

Phase-averaged velocity and vorticity are shown in Figure 31 to Figure 35. For a given oscillation condition, data for 19 phases within the period were acquired. Data for alternate phases, for a total of 10 phases, are shown. The phases, converted to α and direction of pitch, are indicated with each plot. In each of Figure 31 to Figure 35, phase-averaged velocity data are shown at the top (a) and corresponding vorticity data are shown at the bottom (b). Also shown on the lower right corner in each set are the time-averaged distributions at the mean α (=15°) with and without the oscillation. Data are shown for $k = 0.08$, 0.2, and 0.33, with the amplitude $\pm 10°$, in Figure 31 to Figure 33.

Let us first consider the data for the midrange of the parameter space, namely, for $k = 0.20$ and $\alpha = 15° \pm 10°$, as shown in Figure 32. As with the flow visualization, these data are also shown over a

complete period; pairs of plots are chosen at given α with opposite directions of motion, as indicated. Comparing these with corresponding data for the stationary airfoil (Figure 16), some dynamic effects are evident. As noted with the flow visualization data, there is a difference in the distributions with the direction of motion. The vortex structure is seen to be better organized during pitch up. Compare, for example, the distributions in the 16.7°↓ and 16.7°↑ cases; the vortex structure is faint and almost unrecognizable in the pitch-down case whereas it is distinct during the pitch-up case. This difference traces to the flow over the airfoil, which can be quite different between pitch-up and pitch-down states of the oscillation. The phenomenon of "dynamic stall" takes place. During part of the oscillation the flow remains attached, resulting in a coherent tip vortex (well organized), whereas at other times the flow is separated, resulting in a weak and diffused tip vortex.

Differences between pitch-up and pitch-down states in the cycle were also noted in both References 18 and 19 that reported results for a periodically oscillated airfoil. In Reference 18, measurements were carried out with the airfoil oscillated at $k = 0.1$ and $\alpha = 10° \pm 5°$, while in Reference 19, data were reported for $k = 0.18$ and $\alpha = 14° \pm 6°$. Small differences in pitch-up versus pitch-down motions can be seen in the data of Reference 19 (their Figure 5); the vortex core appears to be better organized during the pitch-up motion. However, in Reference 18, a better organized vortex structure is clearly seen during pitch down (their Figure 4), in contrast to the current observation. It appears that this opposite trend is simply a matter of phase lag between events over the airfoil and that noted at the measurement station, which in turn is dictated by the convection velocity of the vortical structures. Whether the vortex is seen more organized during pitch up or pitch down depends on the distance of the observation location, the phase-speed, and the oscillation frequency. A fine numerical study for oscillating (plunging) wing section was recently conducted by Garmann and Visbal (Ref. 31). Variation in the strength and location of the tip vortex at a given downstream location was noted with a varying phase of oscillation, as expected. Under oscillation, they noted a switchover from jet-like to wake-like axial velocity within the vortex core that occurred near the TE of the wing. This was accompanied by a significant enlargement of the core. A similar observation was also made in Reference 19. With reference to the discussion of Table I, both works were for a chord Reynolds number of about 2×10^5—a transitional regime where the switchover from the wake-like to jet-like behavior takes place. Thus, a switchover at different phases of the oscillation cycle may not be unexpected due to changes in the α and dynamic effects. In other words, had the simulation been done for a low R_c as is the present case, such a switchover might not take place since the wake-like behavior dominates at low R_c.

Similar comments can be made for the data for the lower (Figure 31) and higher frequency of oscillation (Figure 33). Comparisons among the three frequency cases do not exhibit any dramatic difference. The vortex at its peak strength at the lowest k (see, $\alpha = 5.6°↓$ in Figure 31) is clearly stronger than the corresponding case at the highest k (see, $\alpha = 5.6°↑$ in Figure 33). There are minor differences in both velocity and vorticity distributions among the three frequency cases. The time-averaged data under the oscillation ("time-avg." 15±10) is the distribution if all the phase-locked distributions for a given case were summed and averaged. The stationary case data at the mean α ("time-avg." 15±0) are also shown for comparison. A distinct tip vortex structure is seen even under the oscillation in the time-averaged flow. The velocity deficit is more pronounced relative to the stationary case at all three frequencies; it is as if this distribution is weighted more by conditions at larger α values. At all k, the oscillation has resulted in a somewhat lower "ω_X-peak" relative to the stationary case. Finally, similar data for two other amplitudes, but for $k = 0.2$, are shown in Figure 34 and Figure 35. Similar comments as with Figure 31 to Figure 33 apply. With the larger amplitude case (Figure 35), the vortex cross section is larger and the vorticity is diffused. Comparing with Figure 32, a systematic progression of such effect is observed; with an increasing amplitude of oscillation, the vortex becomes diffused and its cross section enlarges.

As stated earlier, digital files of all data accompany this report. It is hoped that these experimental results will be useful in future numerical simulation efforts.

Summary of Results

The main inferences are enumerated as follows:

(1) Streamwise vorticity (ω_X) is a superior descriptor of the tip vortex, although mean velocity or turbulence intensity also identifies its location and overall shape.

(2) For the present conditions, the vortex is laminar until an angle of attack (α) of about 16°, but becomes turbulent at higher α. The transition is accompanied by a sharp rise in the turbulence intensity in the vortex core, while both peak vorticity and the axial velocity within the core go through sharp drops in magnitudes. These sharp changes are apparently tied to the onset of stall.

(3) With increasing α, peak vorticity within the core reaches a maximum at about $\alpha = 10°$, stays constant over a range, and then drops off around $\alpha = 16°$ when transition to turbulence occurs.

(4) For all instances examined, the vortex core is characterized by a mean velocity deficit (i.e., a "wake-like" profile). Regions above and below the vortex core are usually marked with excess velocities ("jet-like" profiles) especially at small values of α. The velocity deficit within the core appears to originate from the wake of the airfoil, a part of which gets trapped within the core. The excess velocities outside the vortex core also appear to trace to the U-distribution near the leading edge (LE) of the airfoil.

(5) A comparison with datasets from the literature for $\alpha = 10°$ and for NACA0012/ NACA0015 profiles suggest that 2×10^5 to 5×10^5 might be a transitional range of the chord Reynolds number (R_c) above and below which the axial velocity within the vortex core becomes jet-like or wake-like, respectively.

(6) With square and rounded tips, the overall velocity and vorticity fields look alike. Peak vorticity with the rounded cases is larger, although the net circulation (Γ) for the two tip shapes are almost the same. Some of the winglets explored in the study have a large impact on the flow field. For example, a downward pointing winglet produces a split vortex with significant decrease in peak vorticity. Net Γ, again, does not exhibit significant differences from case to case.

(7) With periodic pitching oscillation, data at $x = 3.2$ are documented. The flow field at a given α exhibits large differences between pitch-up and pitch-down motions within the cycle. Similar observations were made in two prior works reported in the literature. Whether the tip vortex structure is more organized during pitch up or pitch down depends on the distance of the measurement station, phase speed, and the frequency of oscillation.
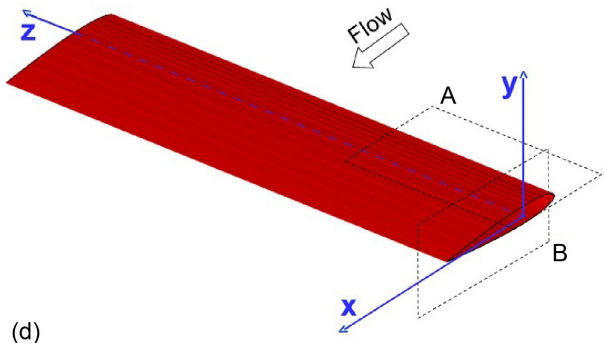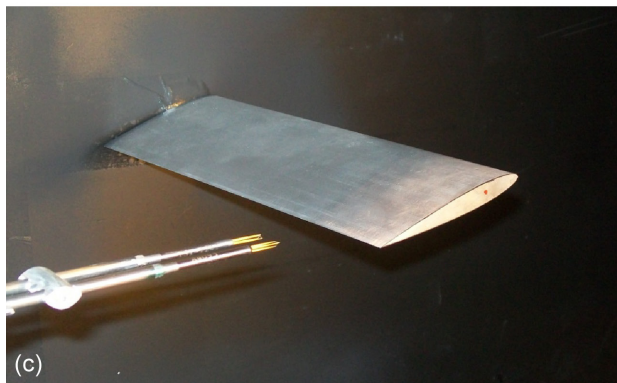
Figure 1.—Experimental facility. (a) Wind tunnel with setup for flow visualization. (b) Airfoil oscillation mechanism. (c) Airfoil inside test section with two crossed hot-wire probes downstream. (d) Airfoil with coordinate system.
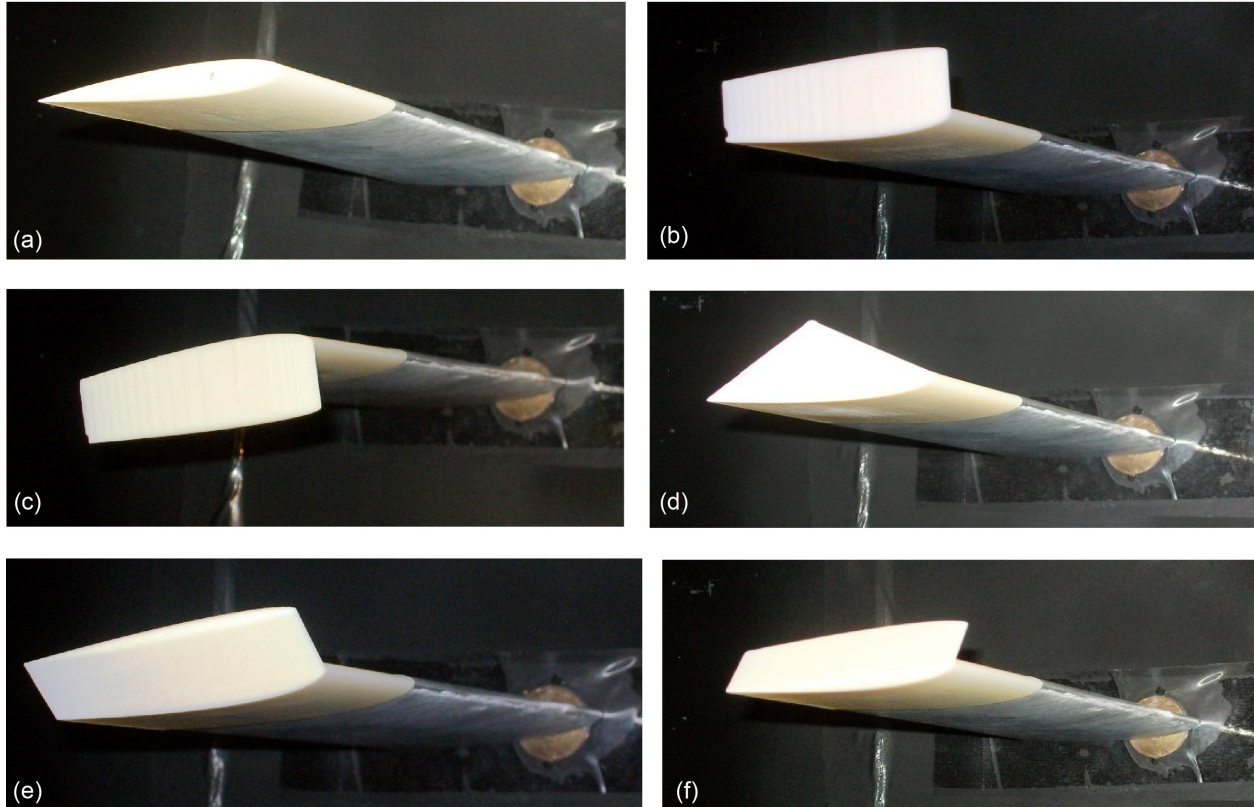
Figure 2.—Various tip shapes for the airfoil. (a) Square or rounded tip (two detachable pieces). (b) Rectangular winglet up. (c) Rectangular winglet down. (d) Triangular winglet. (e) Angled-out winglet. (f) Angled-in winglet.
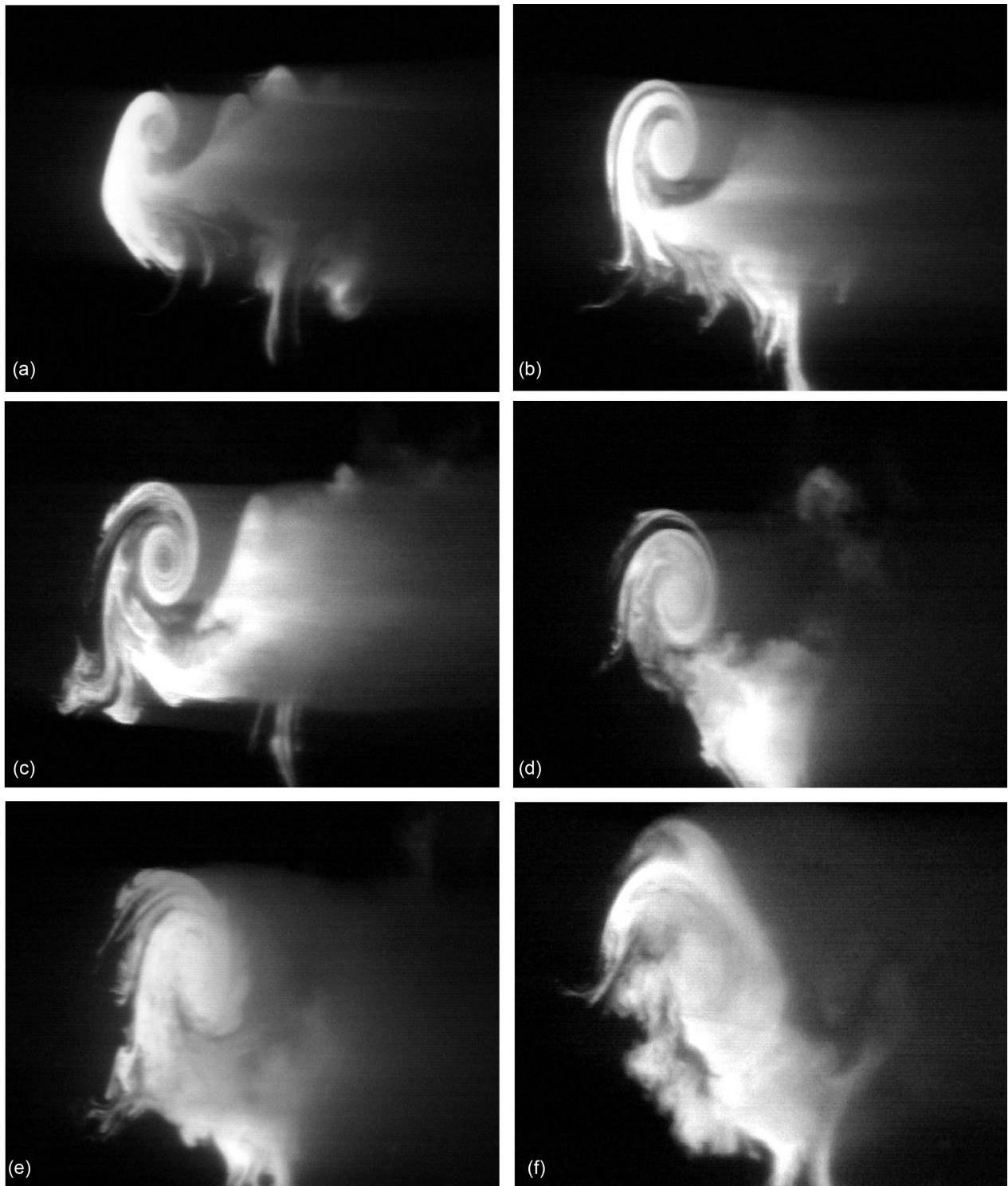
Figure 3.—Laser-sheet illuminated smoke streaks showing cross section of tip vortex at $x \approx 3.2$, for airfoil held fixed at different angles of attack (α). (a) $\alpha = 5°$. (b) $\alpha = 10°$. (c) $\alpha = 15°$. (d) $\alpha = 20°$. (e) $\alpha = 25°$. (f) $\alpha = 35°$.
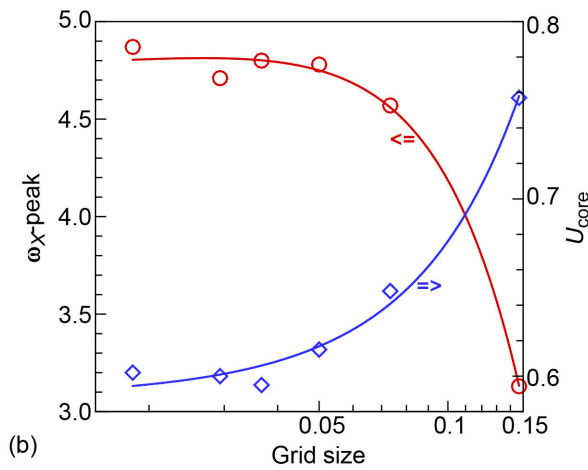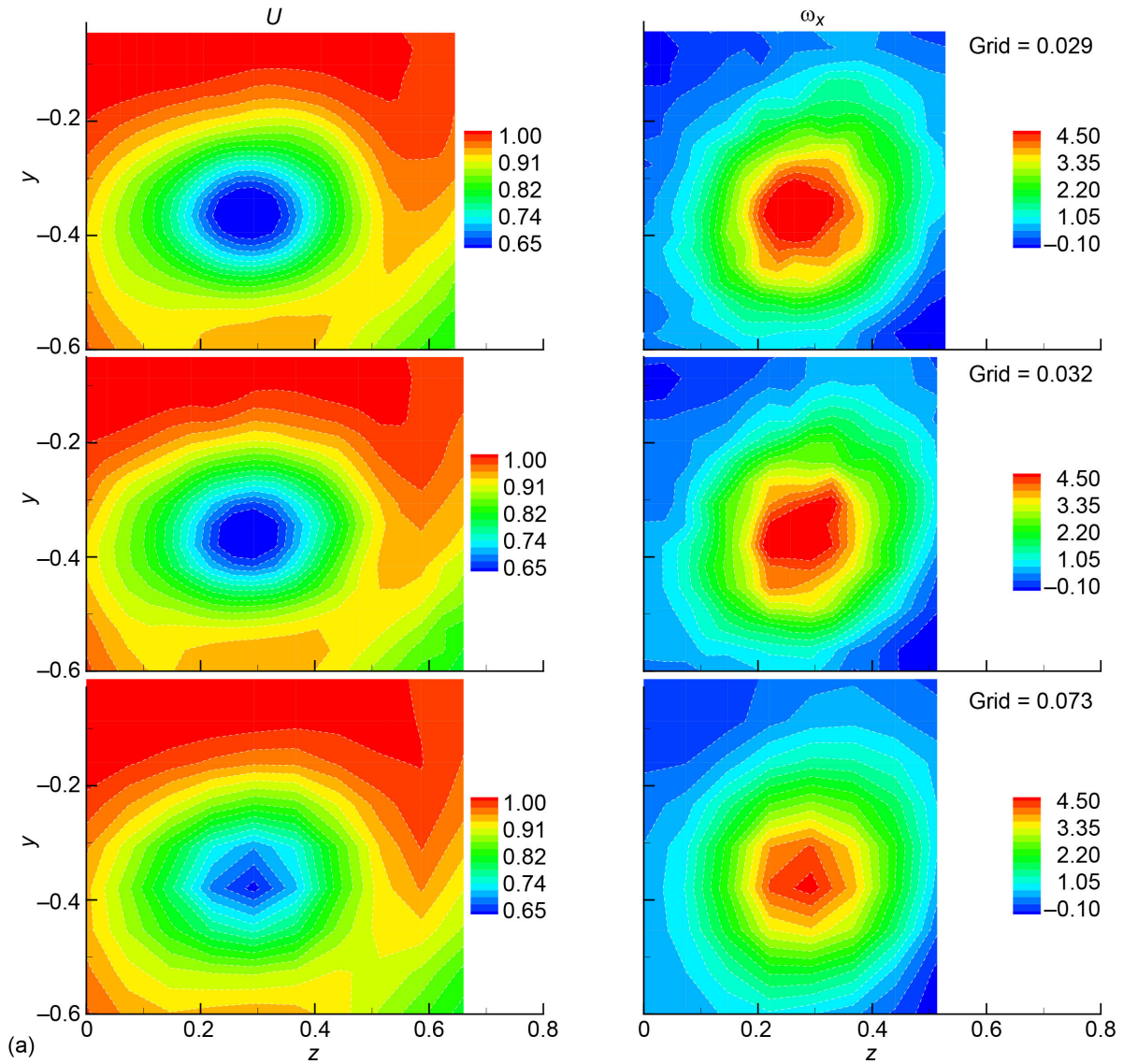
Figure 4.—Measurement grid sensitivity study; x = 3.2, α = 25°. (a) Contours of mean velocity (U) on left and streamwise vorticity (ω_x) on right. Grid size (square) indicated for each row. (b) Maximum vorticity (ω_x-peak, red circles) and minimum velocity (U_{core}, blue diamonds) versus grid size.
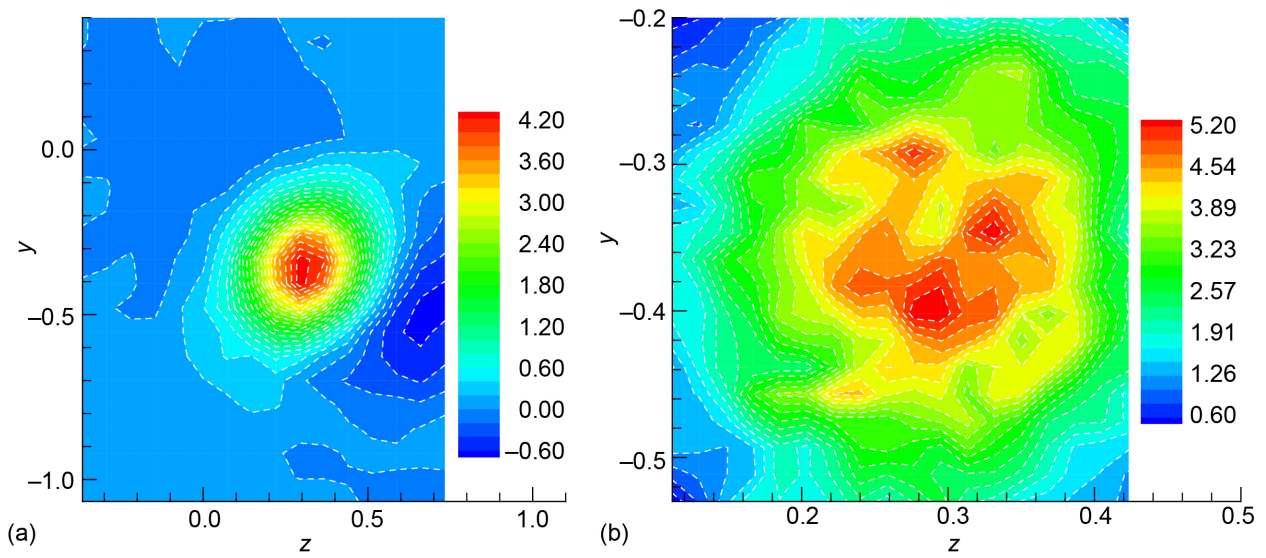
Figure 5.—Distribution of ωx at $x = 3.2$ for $\alpha = 25°$. (a) Measured with coarse grid (0.073). (b) Measured with fine grid (0.018).
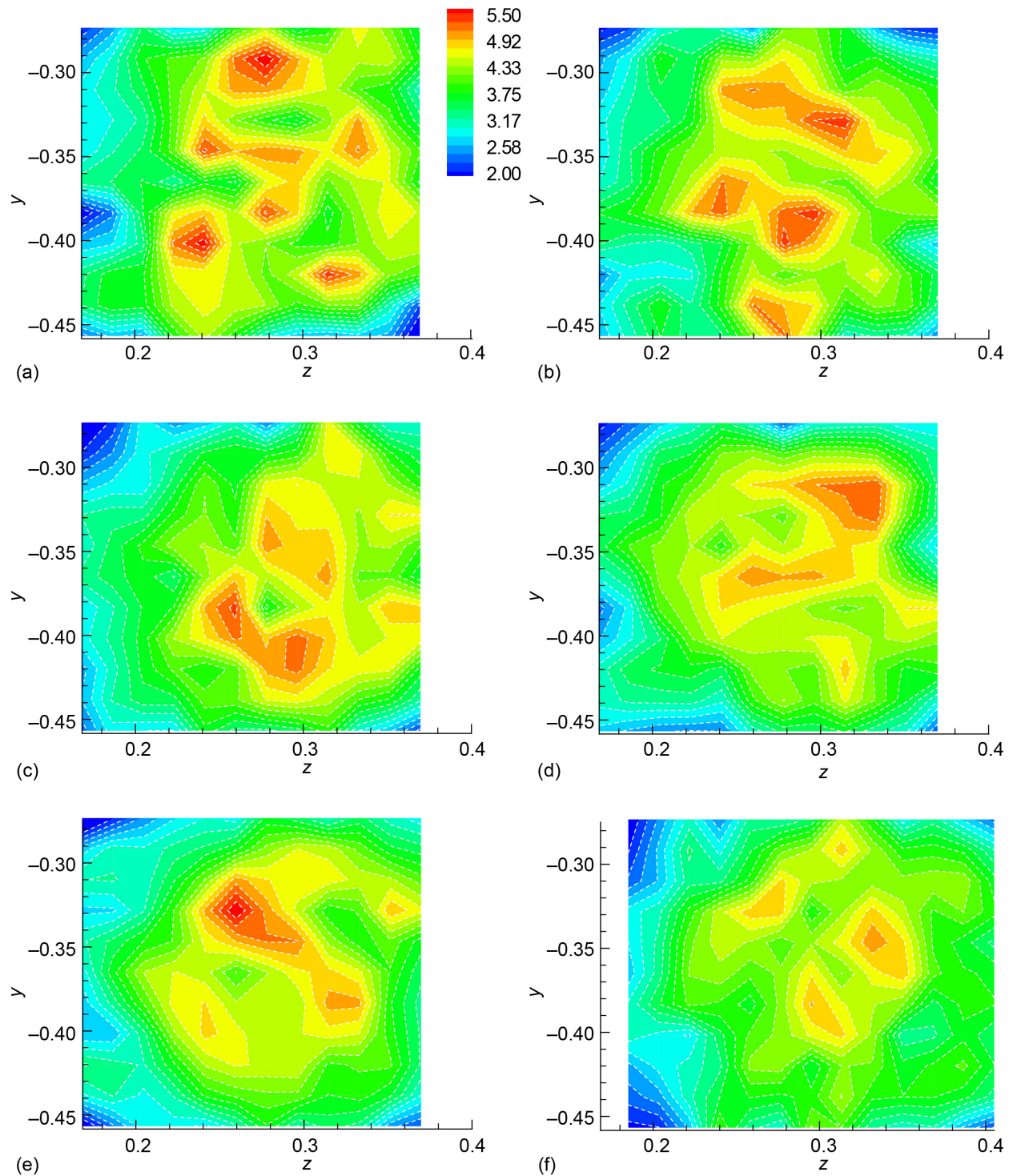
Figure 6.—Lack of repeatability of ωx distribution in the vortex core (0.018 grid); x = 3.2 and α = 25°. Record length for averaging at each grid point. (a) 5 s. (b) 10 s. (c) 10 s repeat. (d) 20 s. (e) 20 s repeat. (f) 50 s.
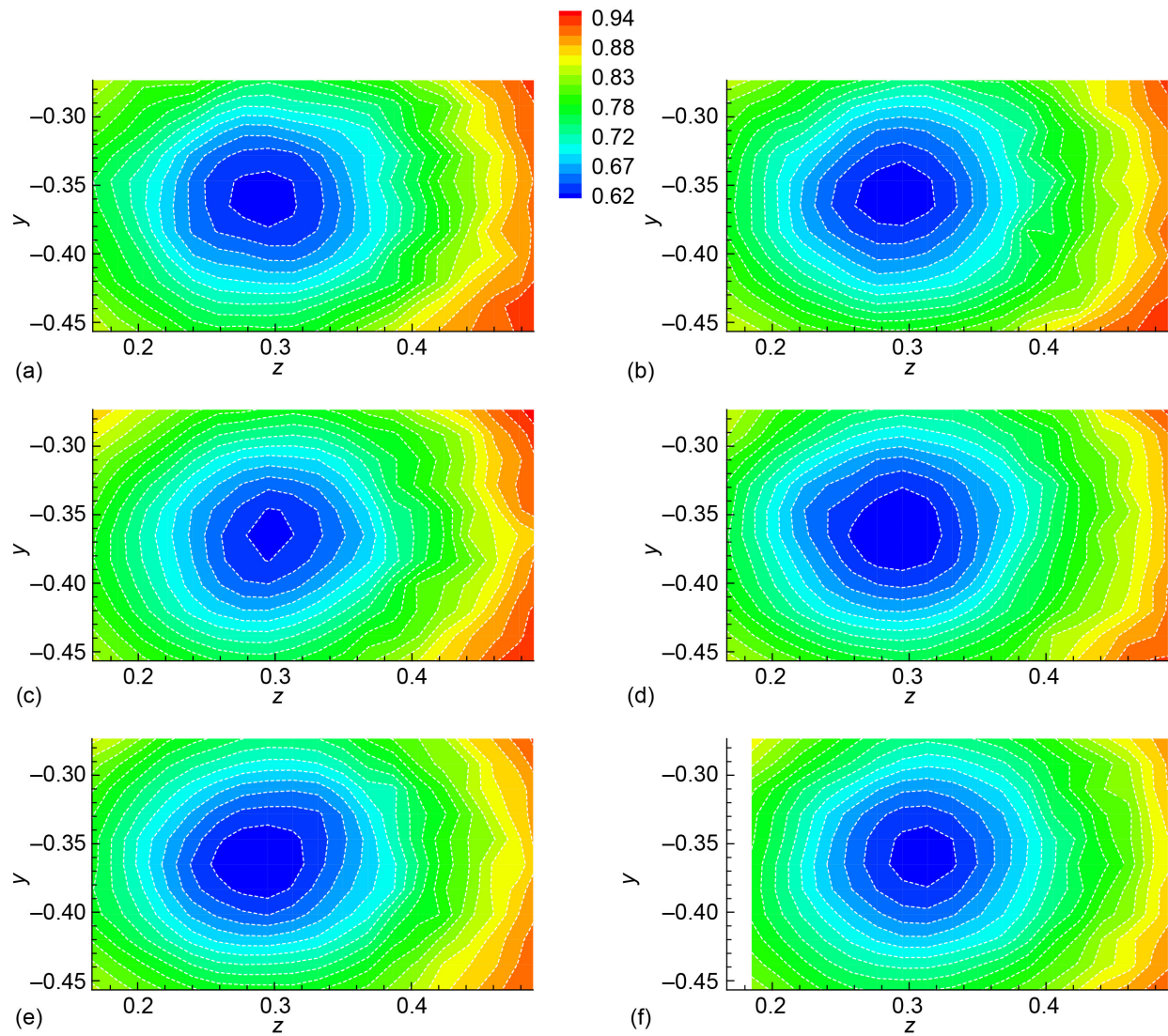
Figure 7.—*U*-distributions corresponding to the same cases as in Figure 6.
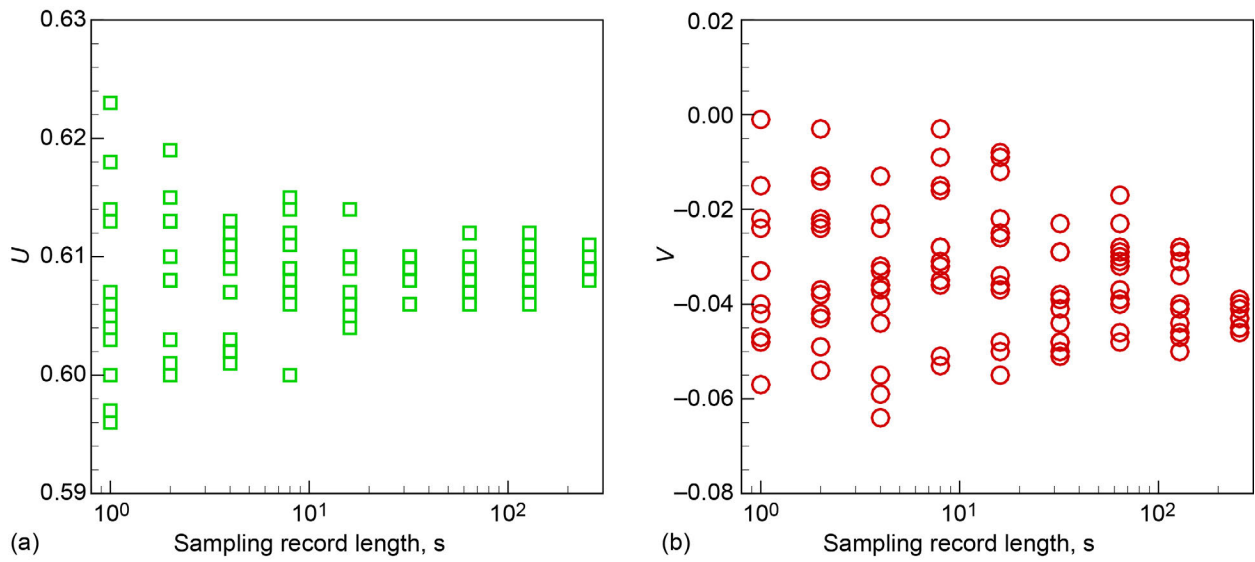
Figure 8.—Scatter in velocity data, measured in the vortex core with varying averaging time; $\alpha = 25°$, $x = 3.2$, $z = 0.31$, and $y = -0.36$. (a) U. (b) V.
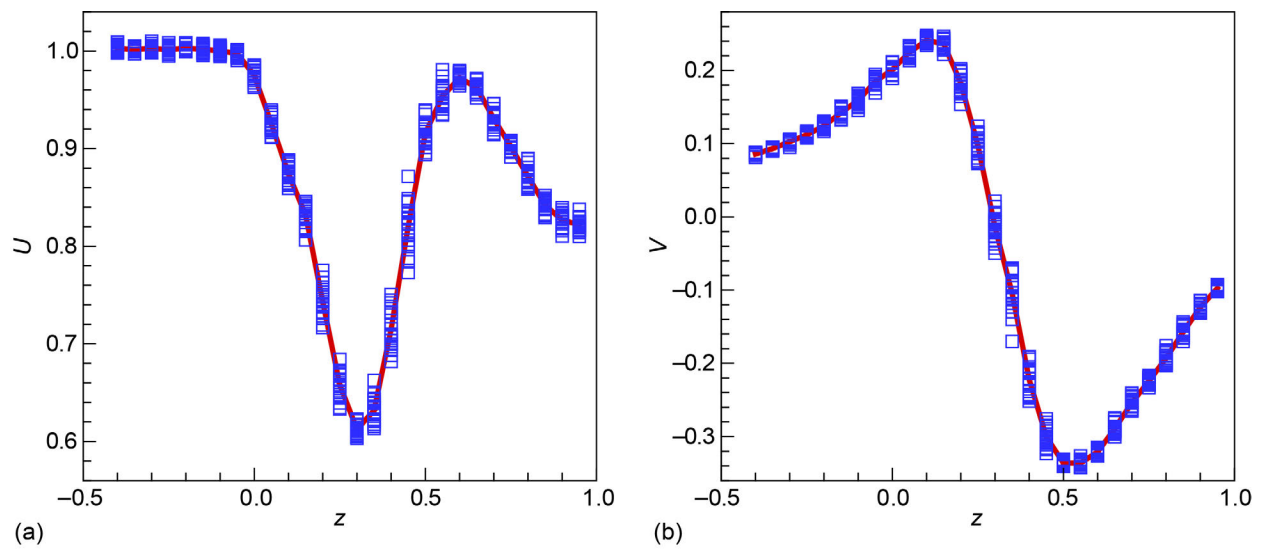
Figure 9.—Velocity profiles through vortex center for 100 s averaging (red curves). Blue symbols for 5 s averaging; $\alpha = 25°$, $x = 3.2$, and $y = -0.36$. (a) U. (b) V.
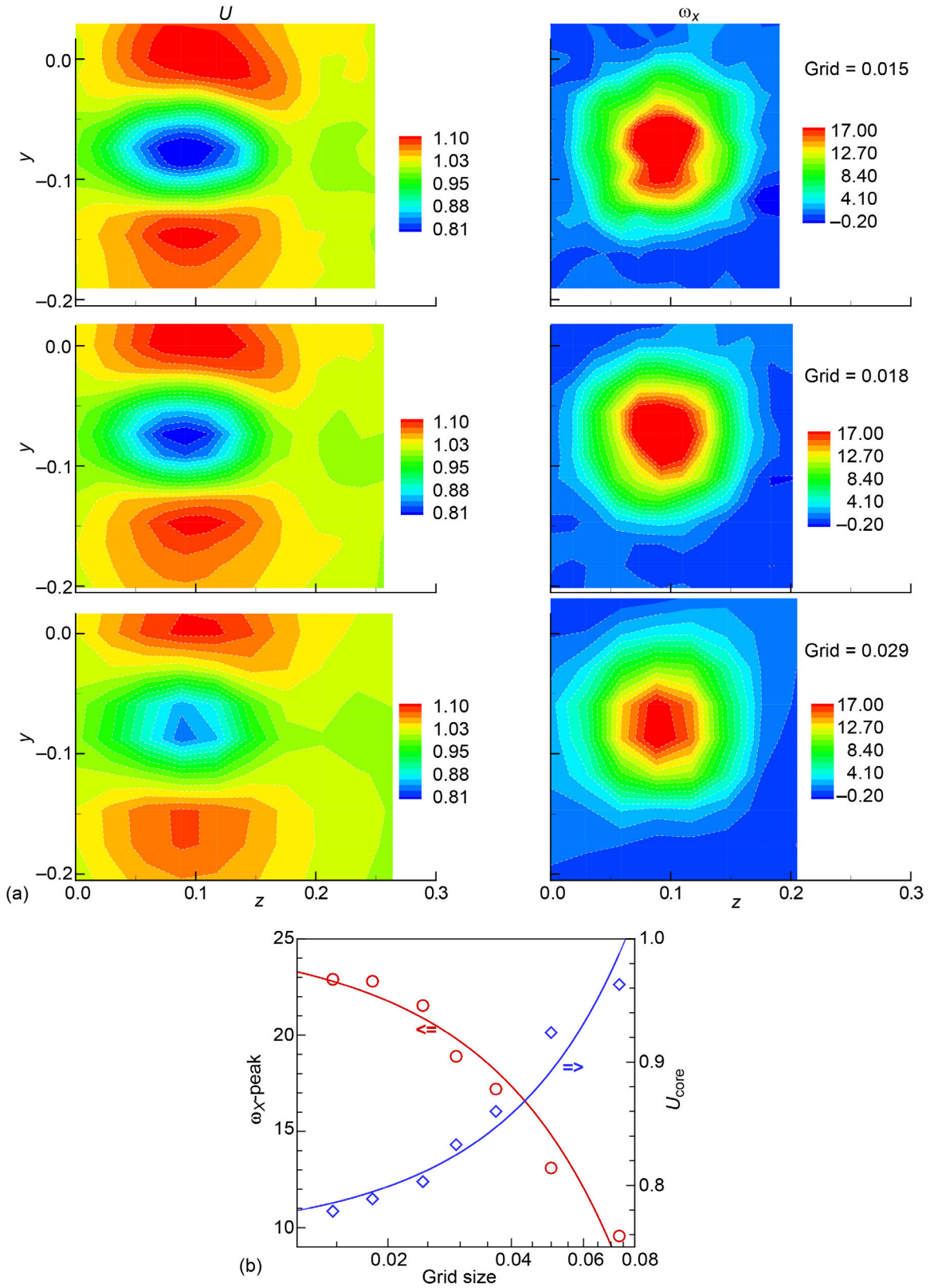
Figure 10.—Measurement grid sensitivity study; x = 3.2 and α = 10°. (a) Contours of mean velocity (U) on left and streamwise vorticity (ω_X) on right. Grid size (square) indicated for each row. (b) Maximum vorticity (ω_X-peak, red circles) and minimum velocity (U_{core}, blue diamonds) versus grid size.

(a)   (b)
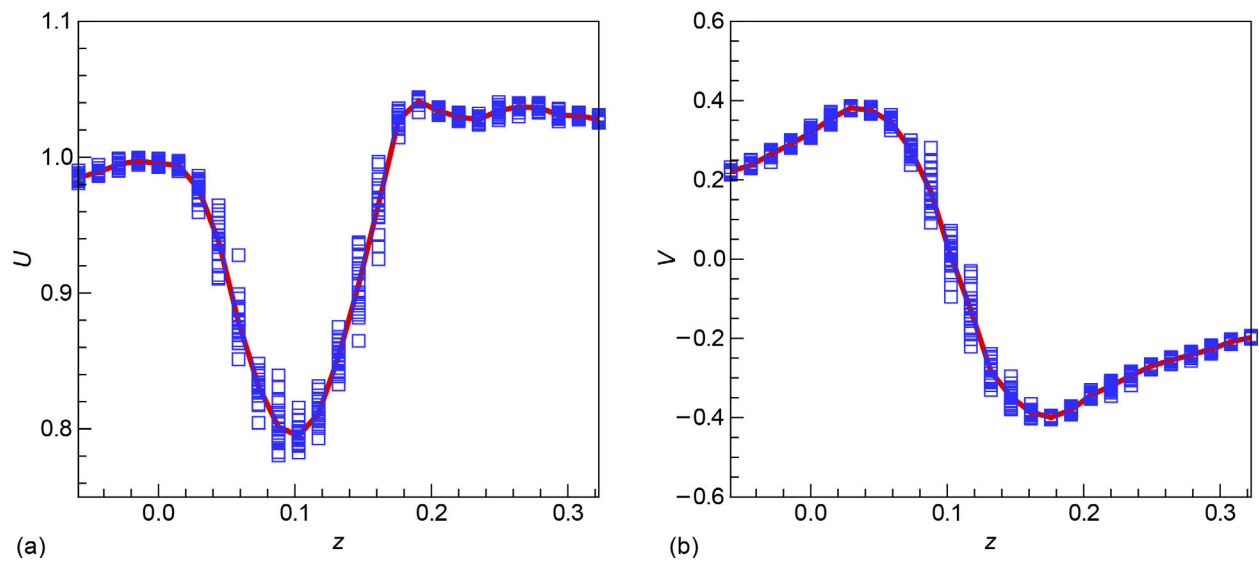
Figure 11.—Velocity profiles through vortex center for 100 s averaging (red curves). Blue symbols for 5 s averaging; $\alpha = 10°$, $x = 3.2$, and $y = -0.073$. (a) U. (b) V.
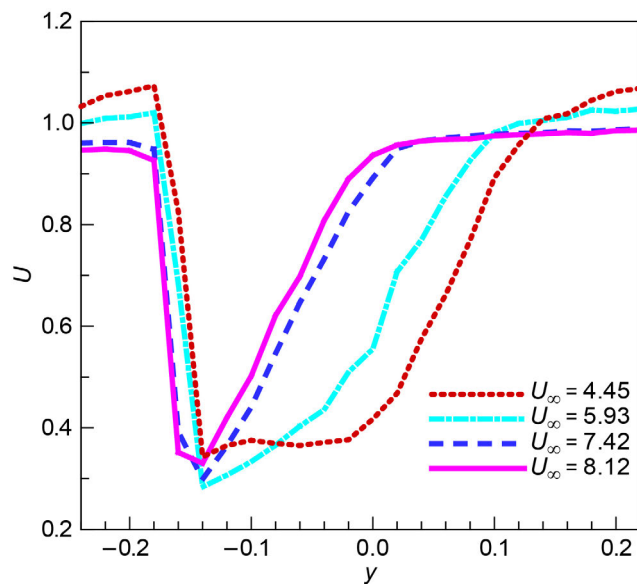
Figure 12.—$U(y)$ profiles just downstream of trailing edge ($x = 0.8$) and away from tip of airfoil ($z = 1.0$) for different freestream velocities (U_∞, m/s); $\alpha = 10°$.
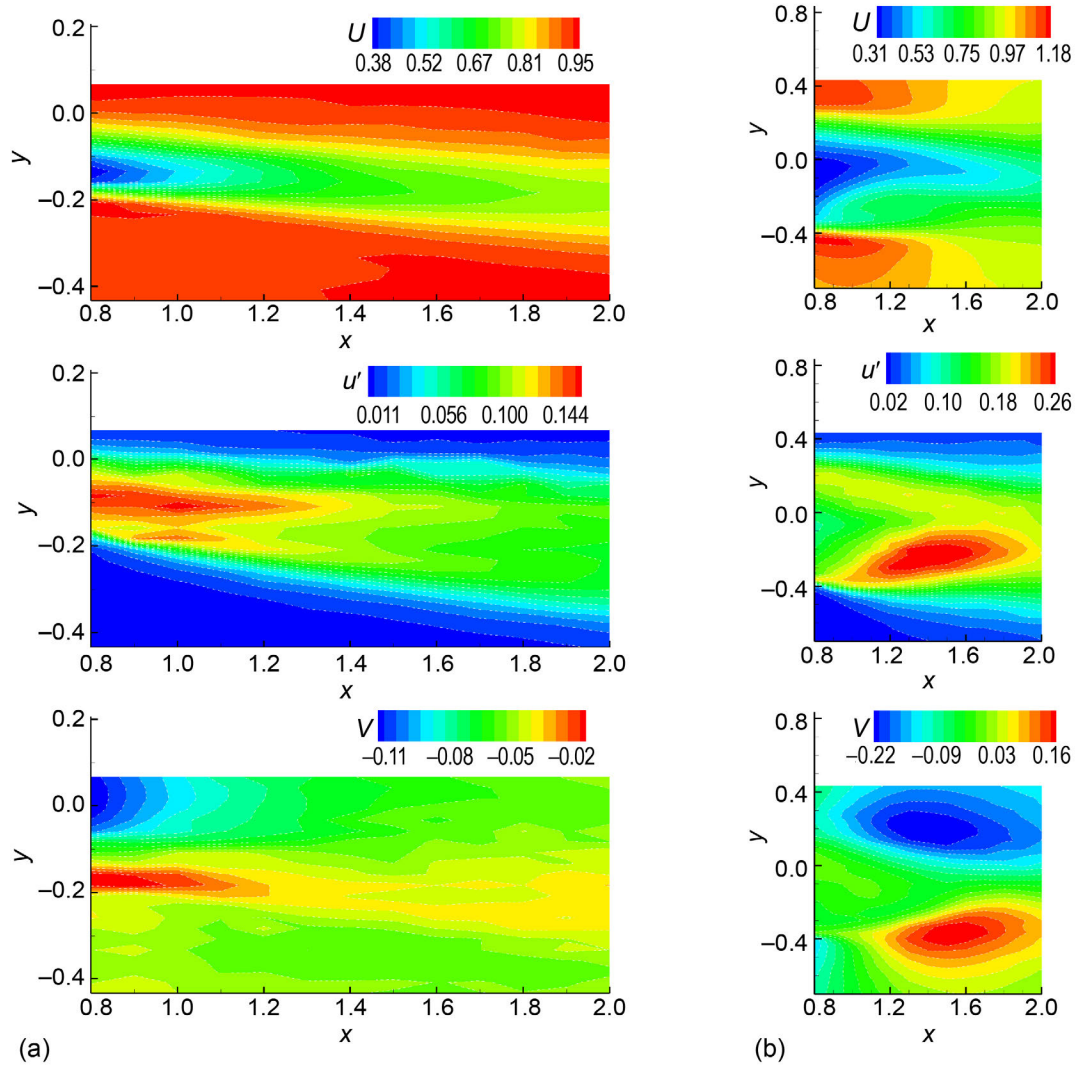
Figure 13.—Wake characteristics at z = 1.0; distributions of U, u', and V on x-y plane.
(a) α = 10°. (b) α = 25°.
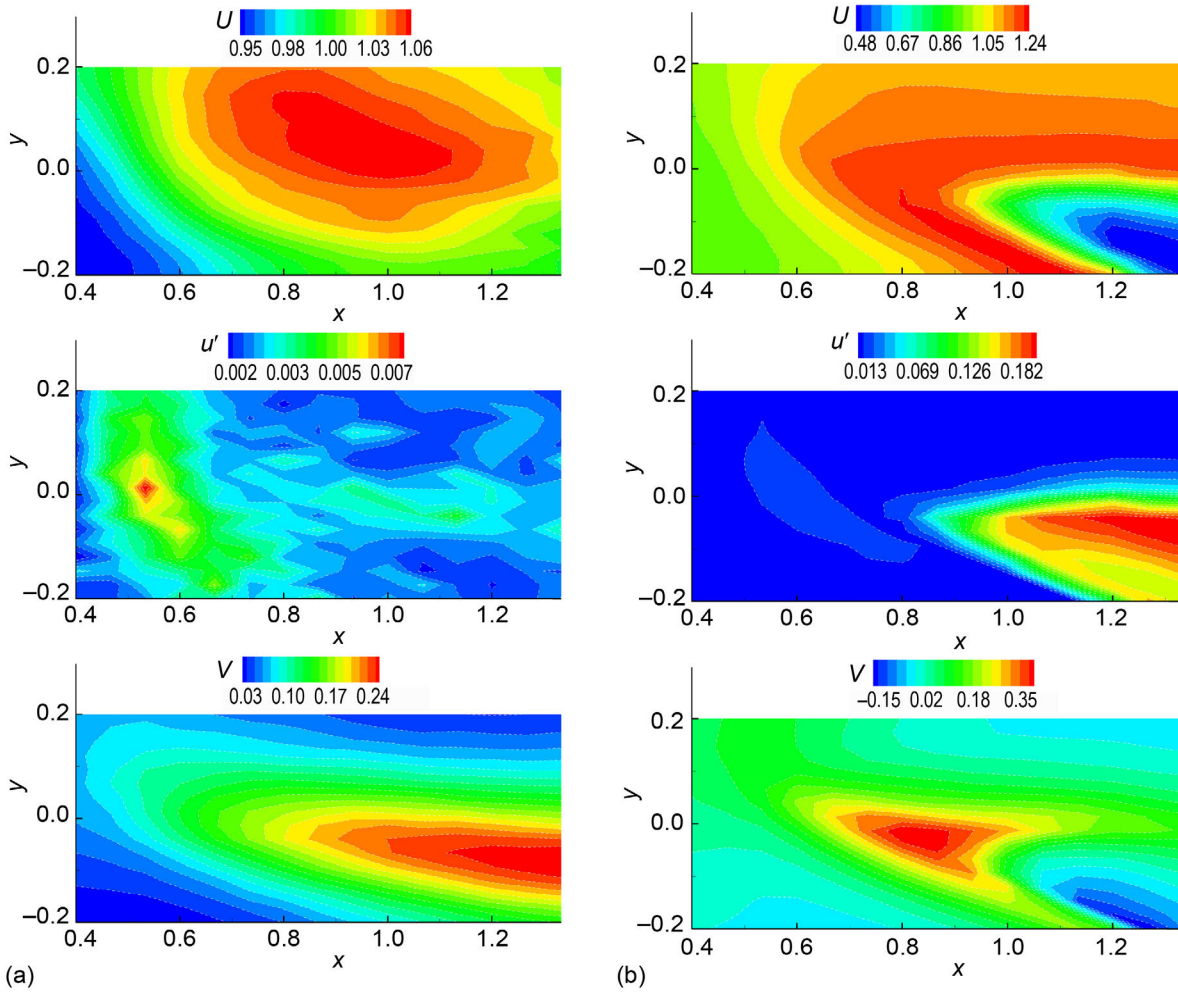
Figure 14.—Distributions of U, u', and V on a vertical (x-y) plane on the side of airfoil tip (plane B in Figure 1(d)) at $z = -0.08$. (a) $\alpha = 10°$. (b) $\alpha = 25°$.
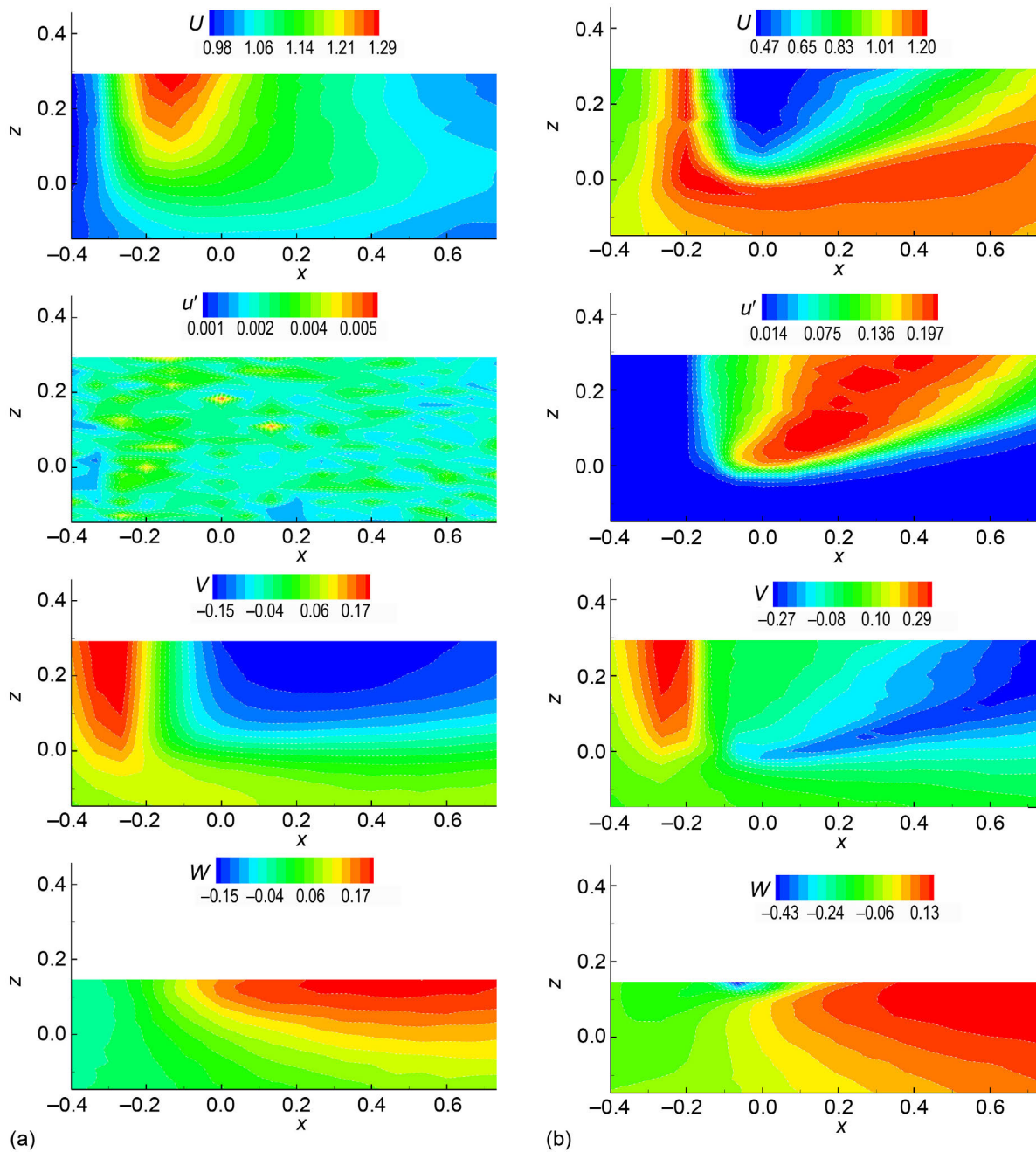
Figure 15.—Distributions of U, u', V, and W on a horizontal (x-z) plane just above the leading edge (LE) (plane A in Figure 1(d)). (a) $\alpha = 10°$ and $y = 0.12$. (b) $\alpha = 25°$ and $y = 0.15$.
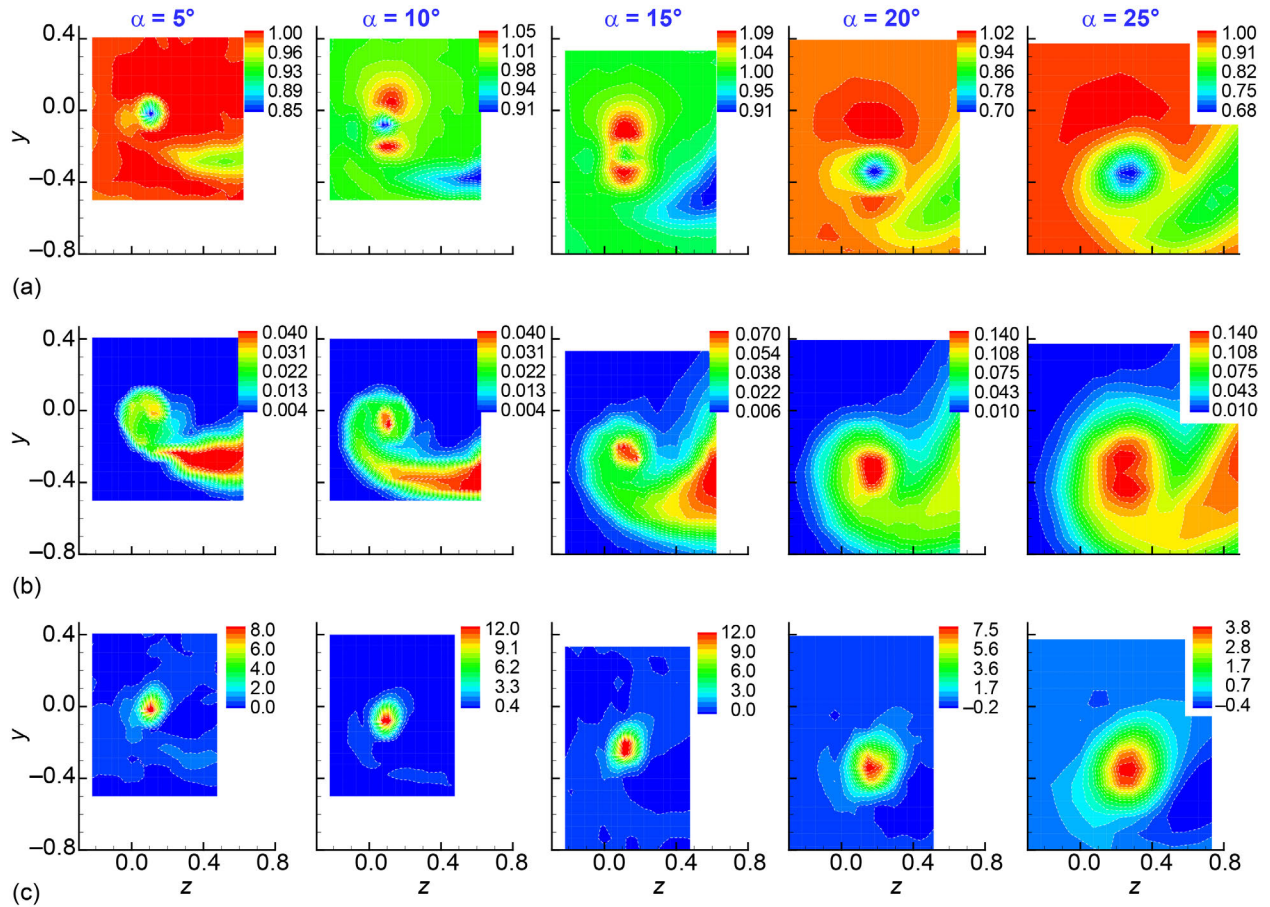
Figure 16.—Distributions of various flow properties on cross-sectional (*y-z*) plane at *x* = 3.2 for different α. Contours of *U*, *u′*, and ω*x* are shown in (a) top, (b) middle, and (c) bottom rows, respectively.
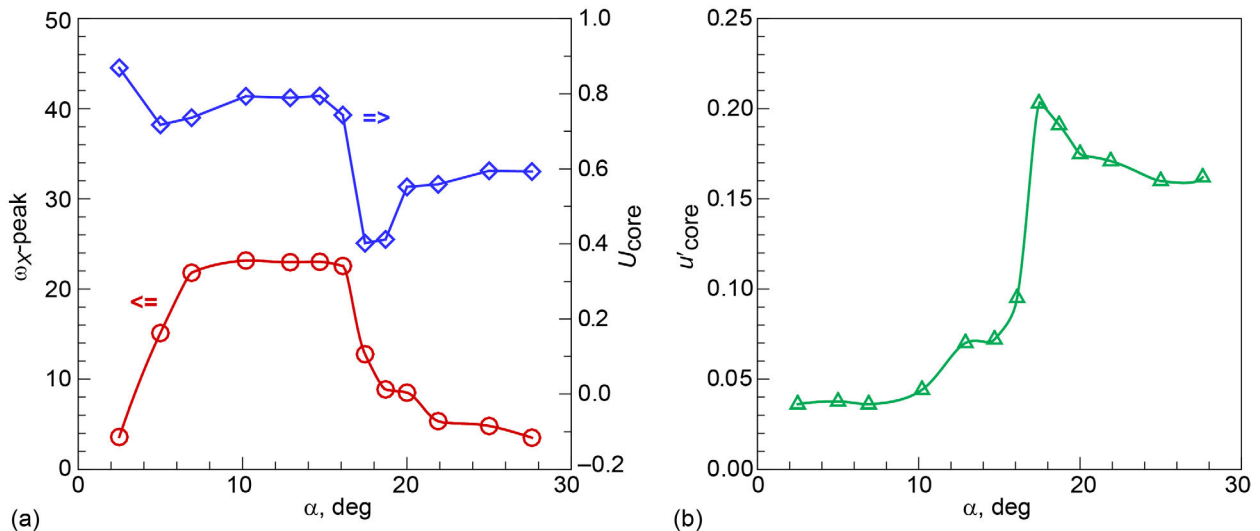
Figure 17.—Maximum of vorticity (ω*x*-peak), minimum of velocity (*U*core) and maximum of turbulence intensity (*u′*core) within vortex core versus α. (a) ω*x*-peak (red circles) and *U*core (blue diamonds). (b) *u′*core.
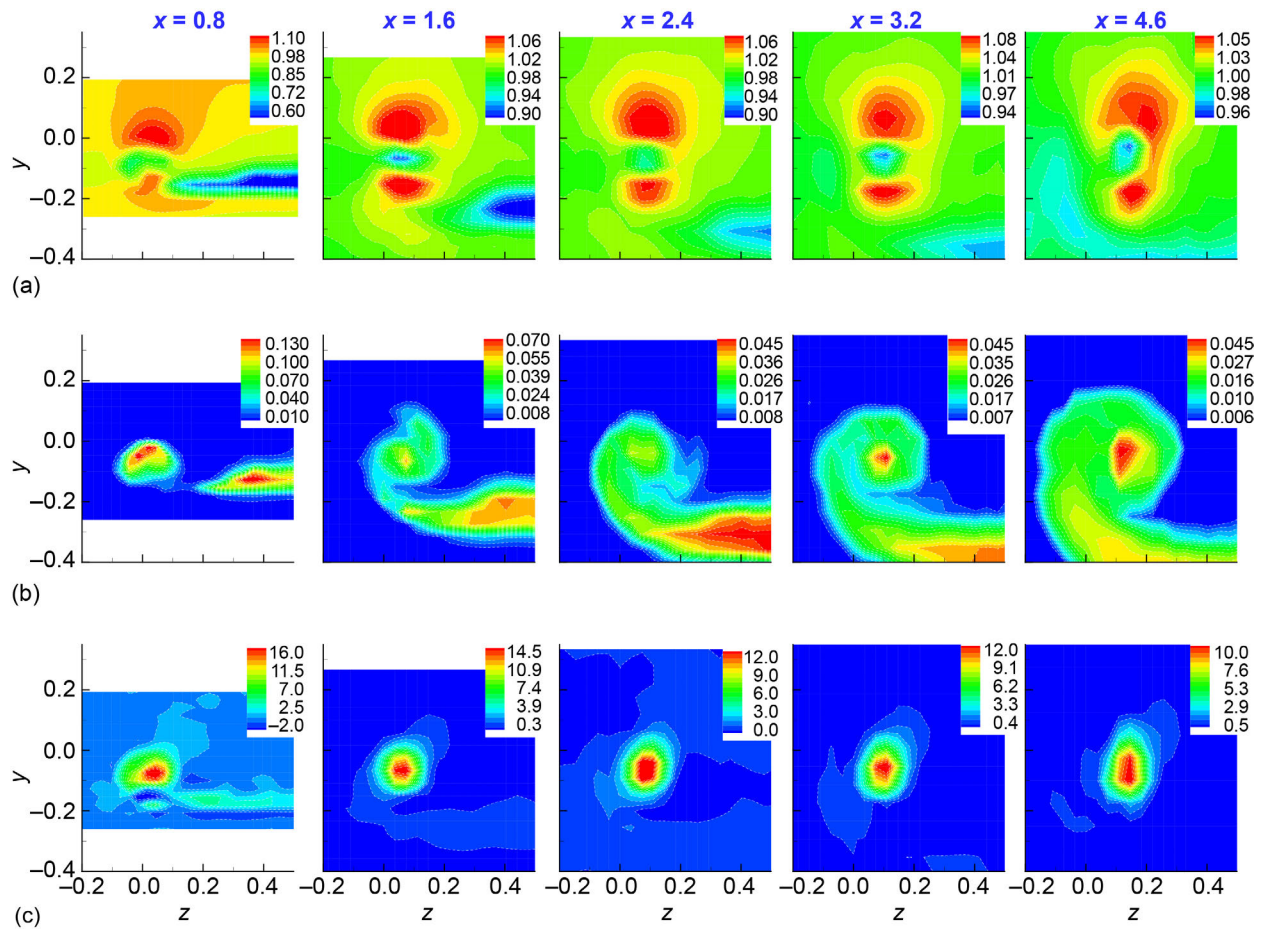
Figure 18.—Distributions of U, u', and ωx on cross-sectional (y-z) plane at different x for $\alpha = 10°$. Contours of U, u', and ωx are shown in (a) top, (b) middle, and (c) bottom rows, respectively.
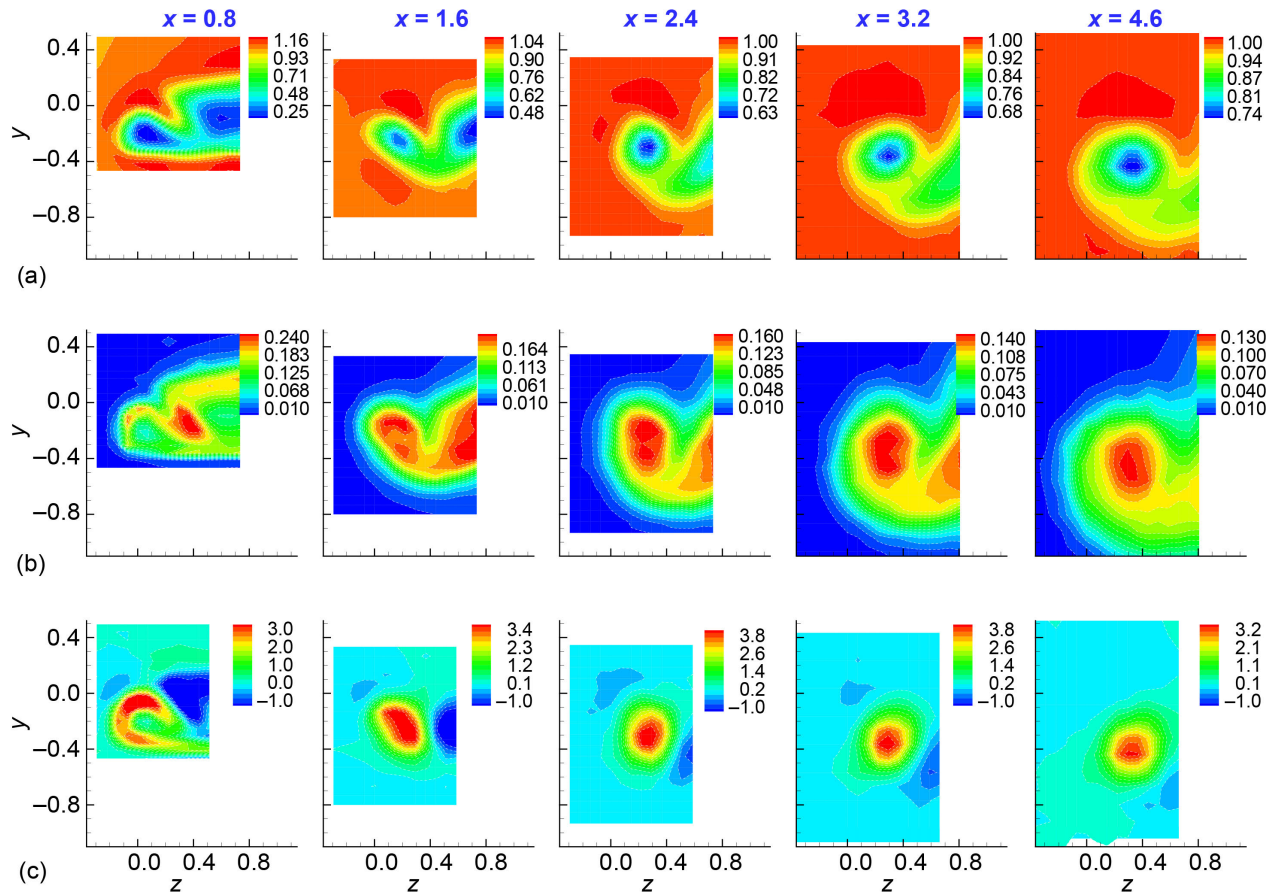
Figure 19.—Distributions of *U*, *u′*, and ω*x* on cross-sectional (*y-z*) plane at different *x* for α = 25°. Contours of *U*, *u′*, and ω*x* are shown in (a) top, (b) middle, and (c) bottom rows, respectively.
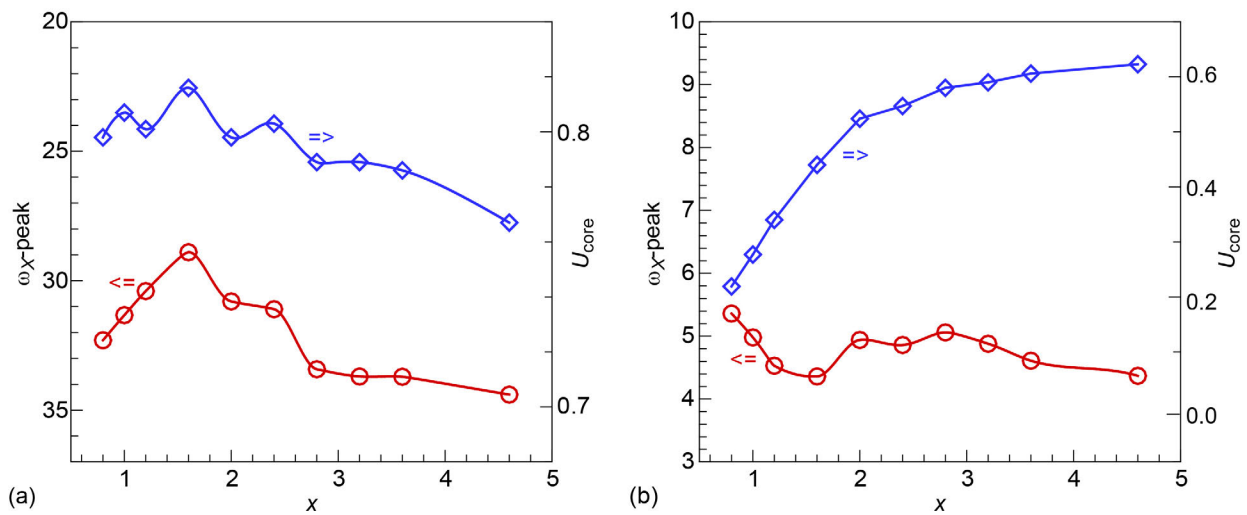
Figure 20.—Values of ωx-peak (red circles) and U_{core} (blue diamonds) versus x. (a) α = 10°. (b) α = 25°.
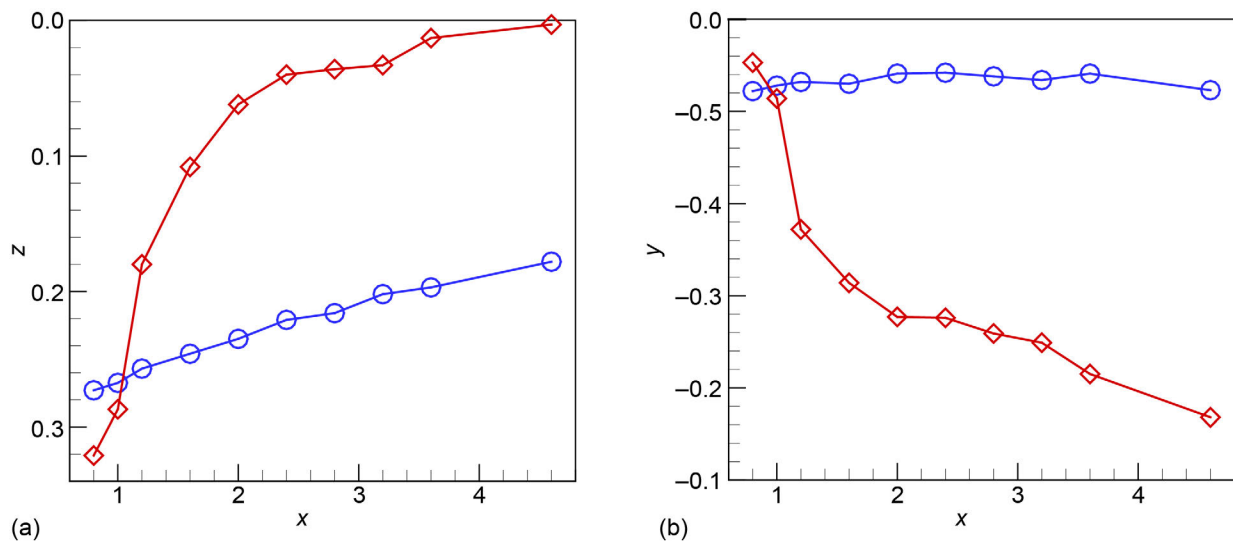
Figure 21.—Trajectory of vortex core. Vortex center locations are shown by (blue) circular symbols for α = 10° and (red) diamond symbols for α = 25°. (a) z versus x. (b) y versus x.
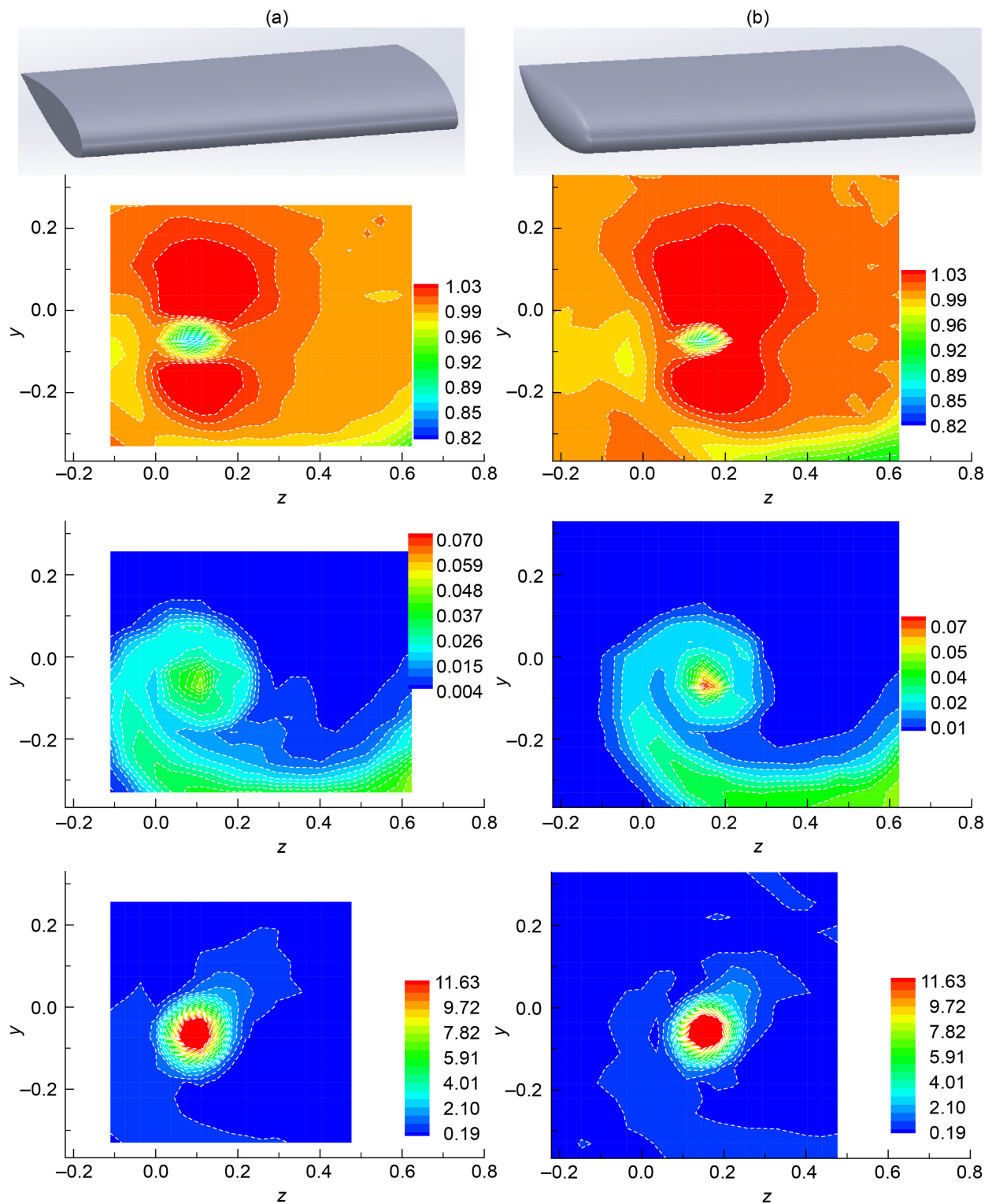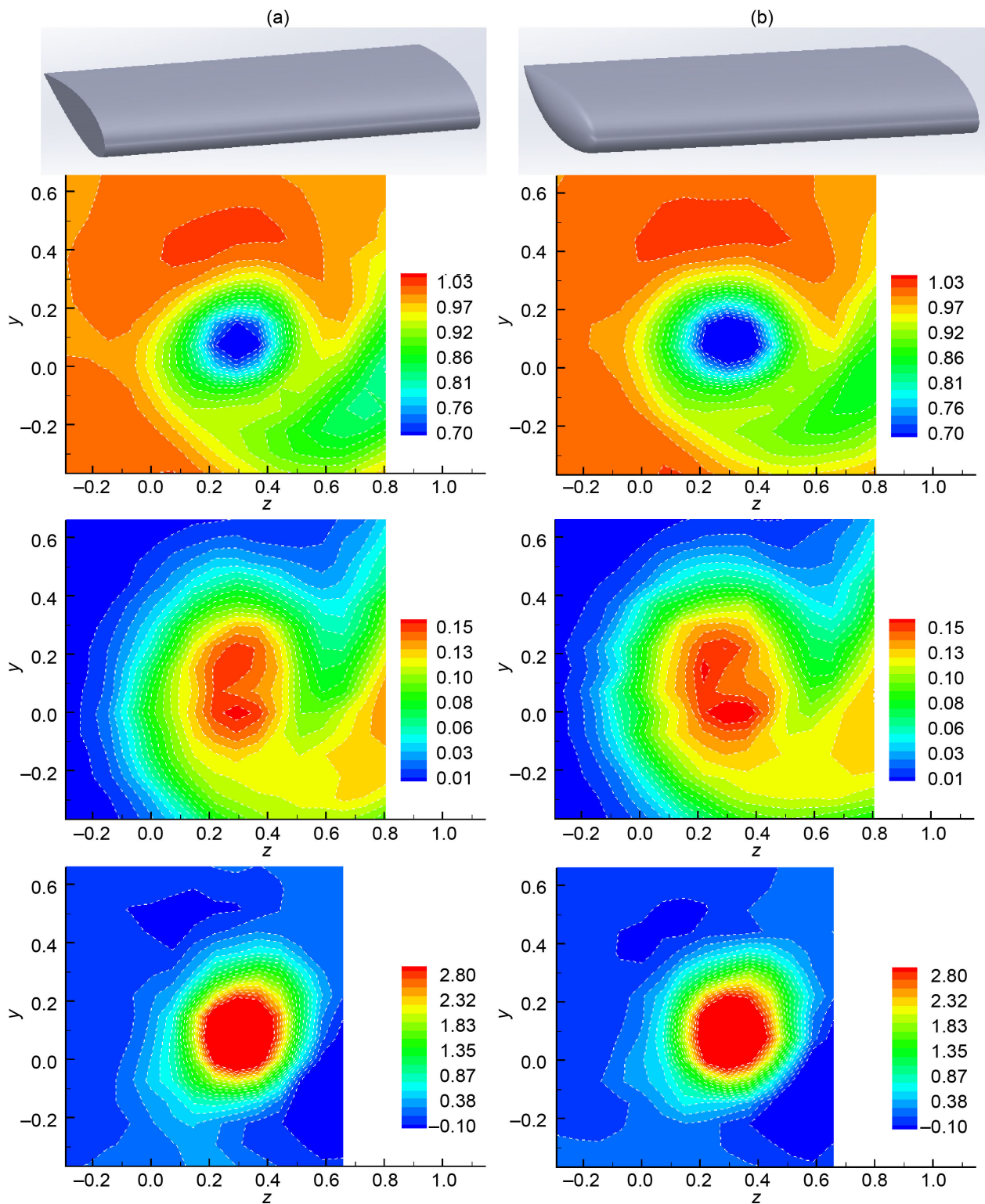
Figure 22.—Tip shape effect at $x = 3.2$ and $\alpha = 10°$. (a) Square tip. (b) Rounded tip. In each column, U, u', and ωx are shown in top, middle, and bottom rows, respectively.
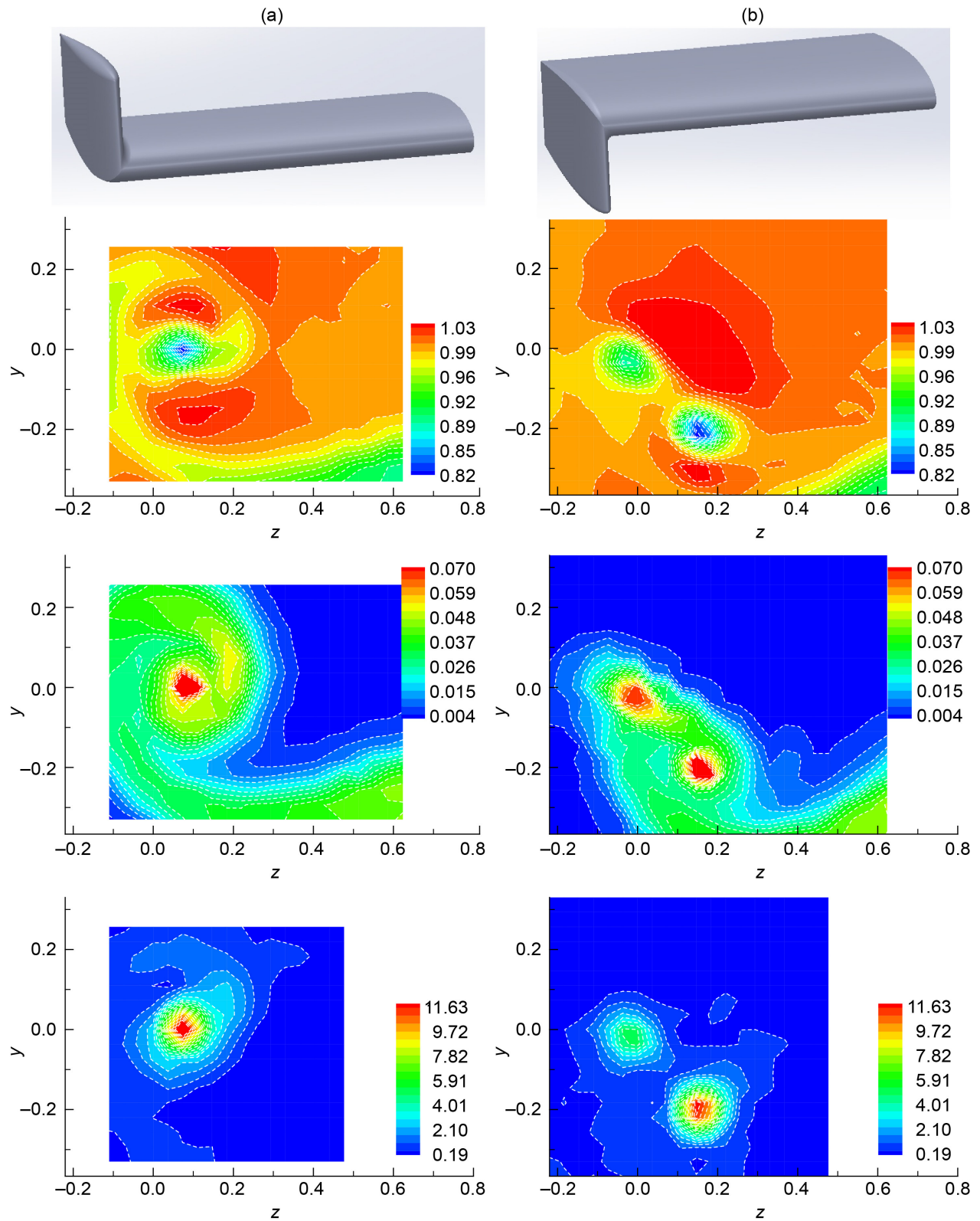
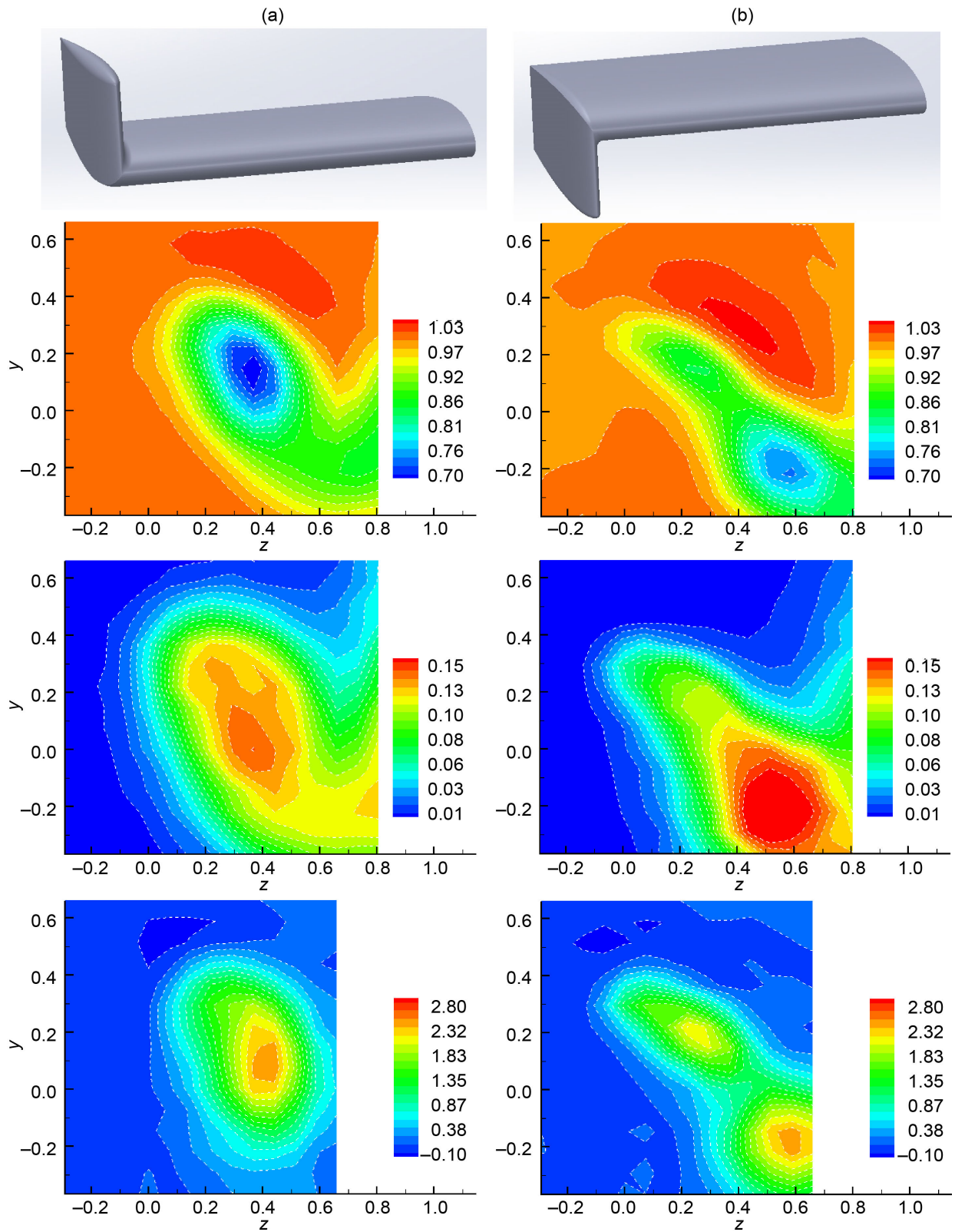Figure 23.—Winglet shape effect at x = 3.2 and α = 10°. (a) Winglet up. (b) Winglet down. In each column, U, u', *and* ωx are shown in top, middle, and bottom rows, respectively.
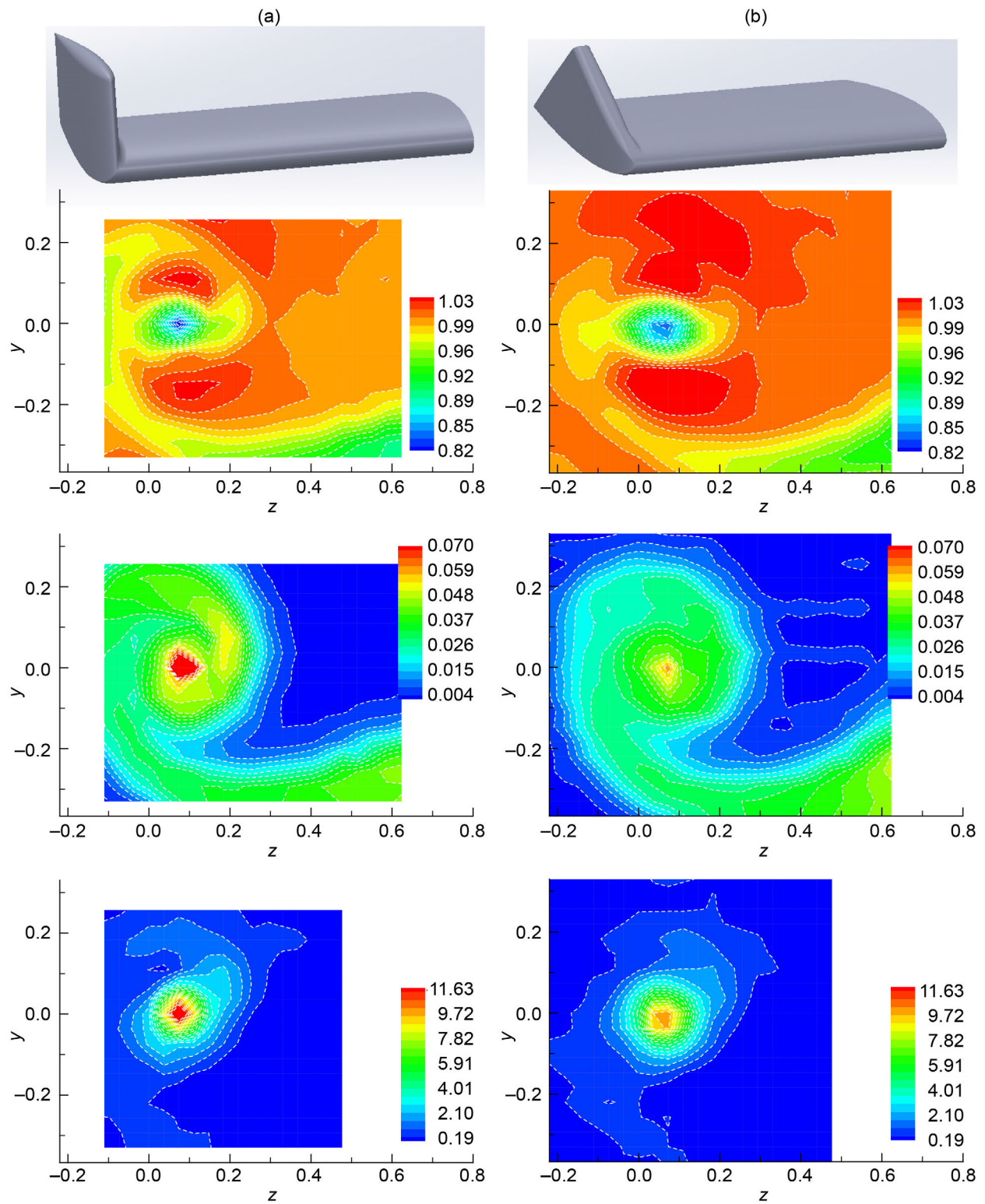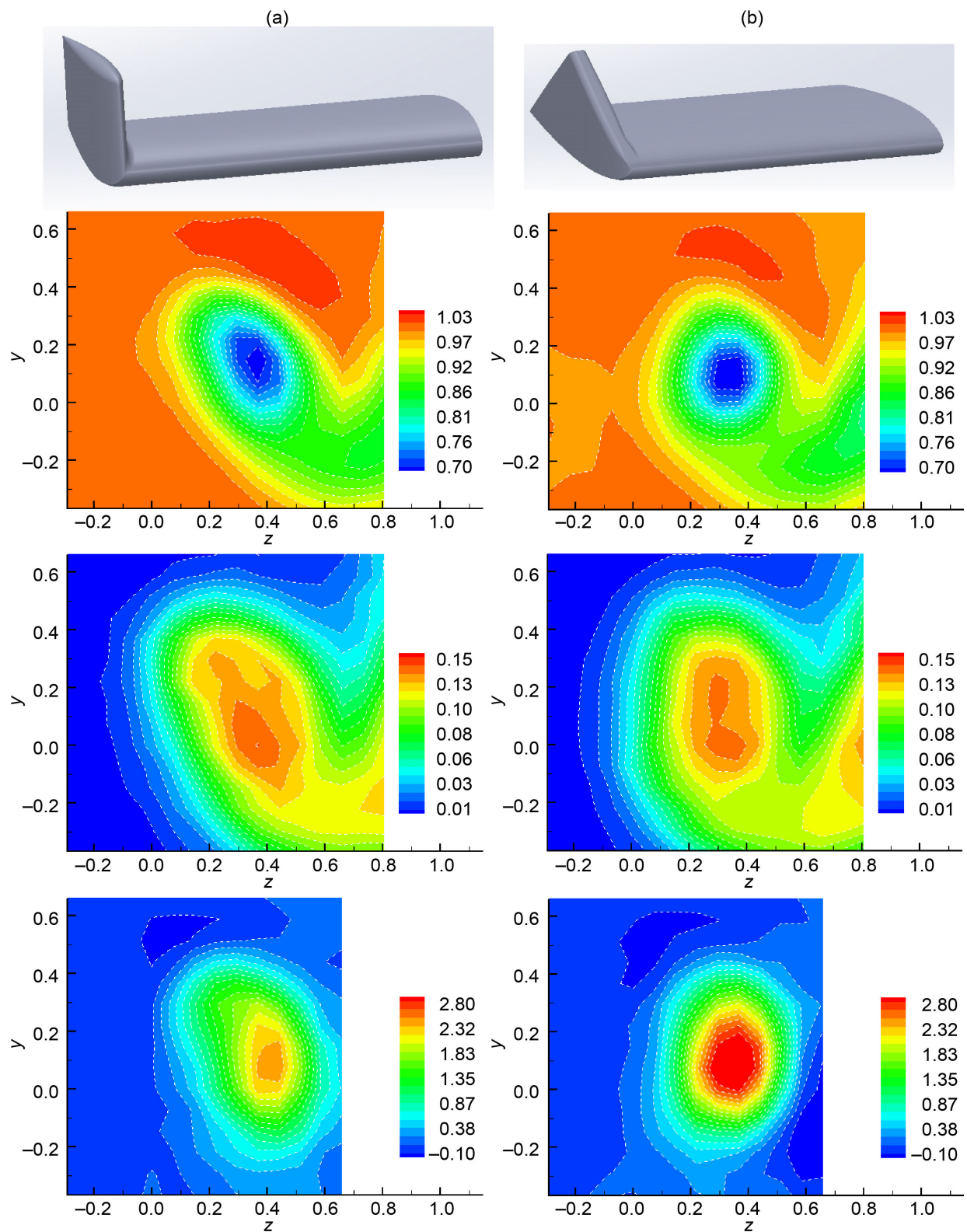
Figure 24.—Winglet shape effect at x = 3.2 and α = 10°. (a) Rectangular. (b) Triangular. In each column, U, u', and ω_x are shown in top, middle, and bottom rows, respectively.
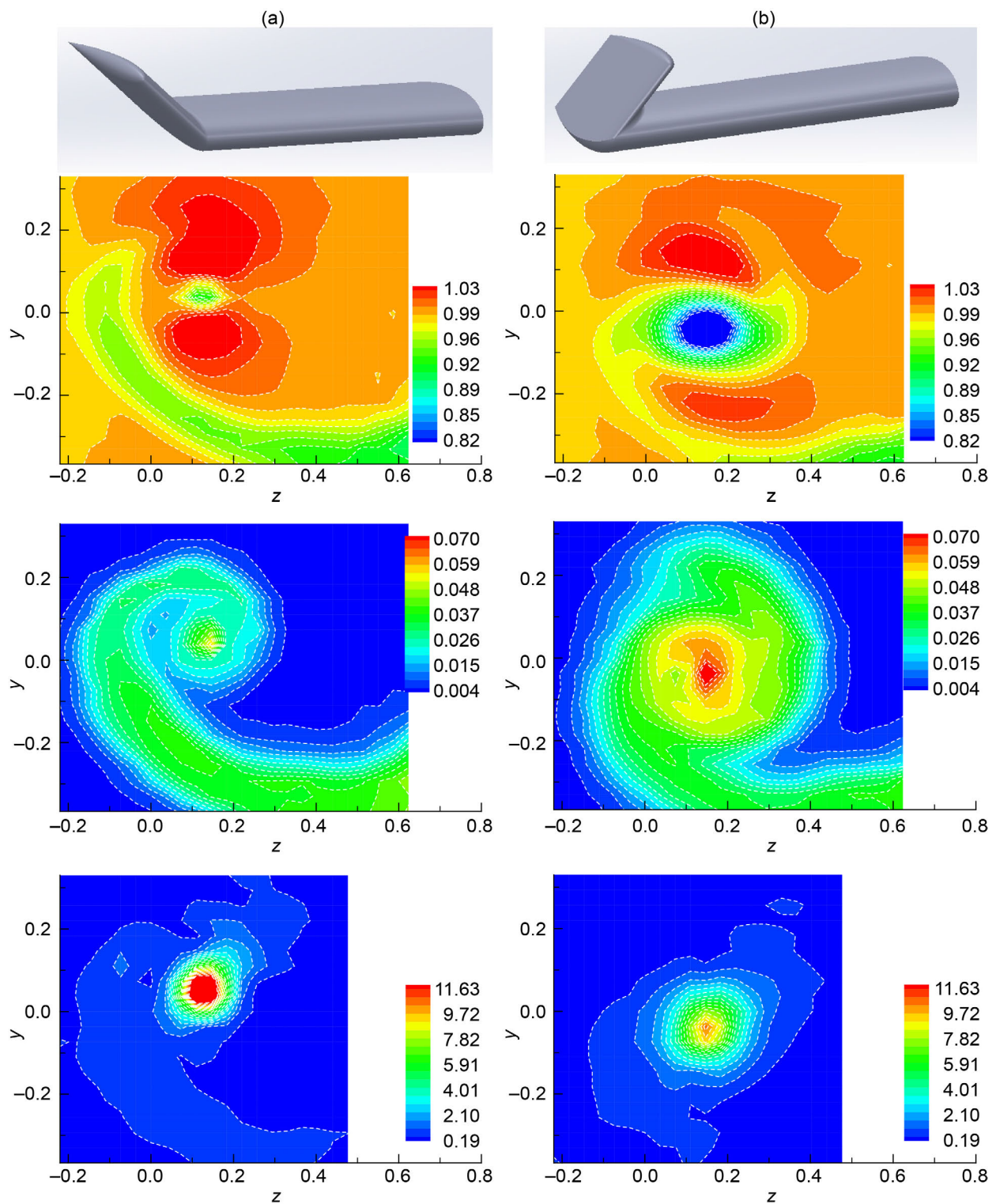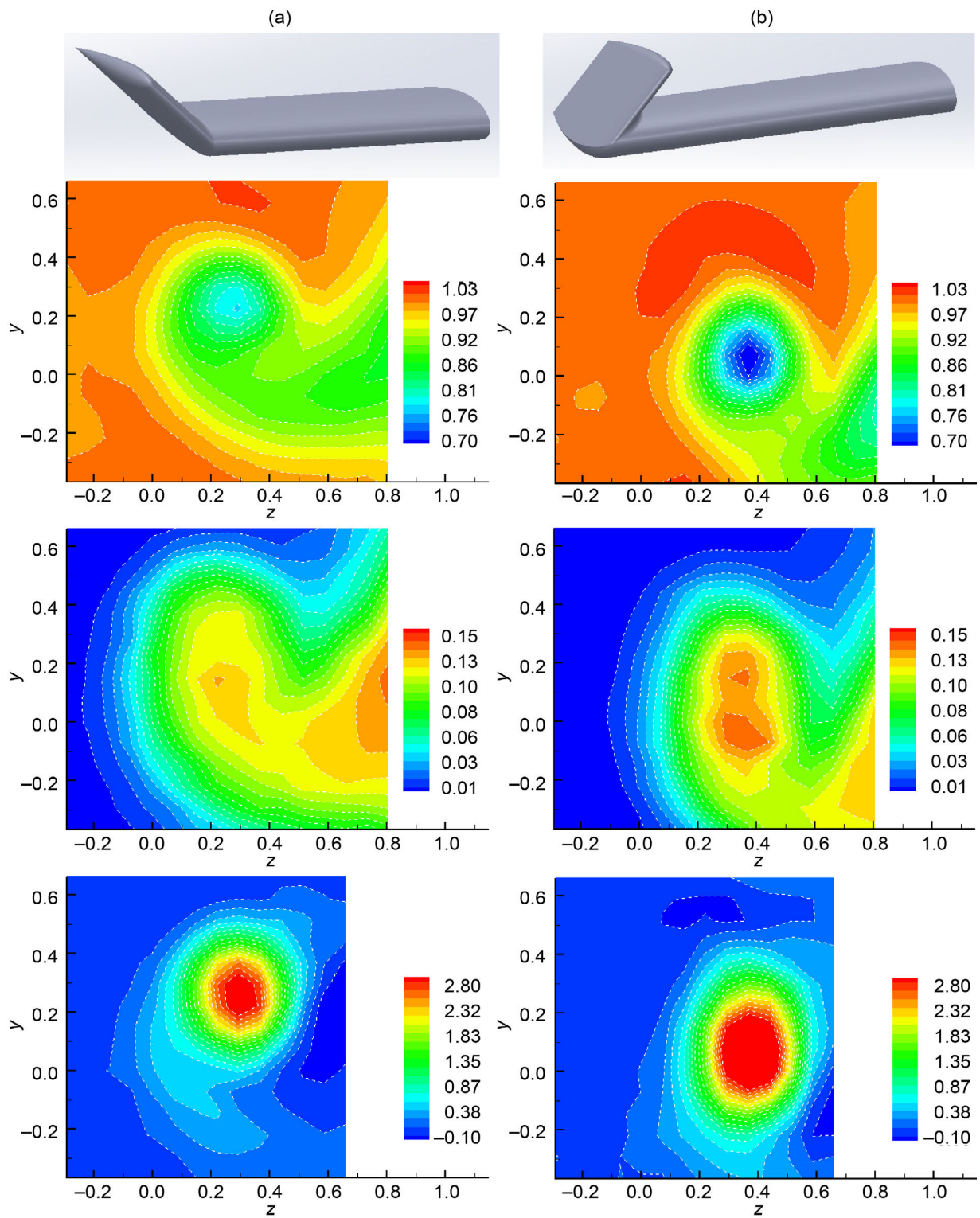
Figure 25.—Winglet shape effect at $x = 3.2$ for $\alpha = 10°$. (a) Angled out. (b) Angled in. In each column, U, u', and ω_X are shown in top, middle, and bottom rows, respectively.

Figure 26.—Tip shape effect at $x = 3.2$ for $\alpha = 25°$. (a) Square tip. (b) Rounded tip. In each column, U, u', *and* ωx are shown in top, middle, and bottom rows, respectively.

Figure 27.—Winglet shape effect at $x = 3.2$ for $\alpha = 25°$. (a) Winglet up. (b) Winglet down. In each column, U, u', and ω_x are shown in top, middle, and bottom rows, respectively.
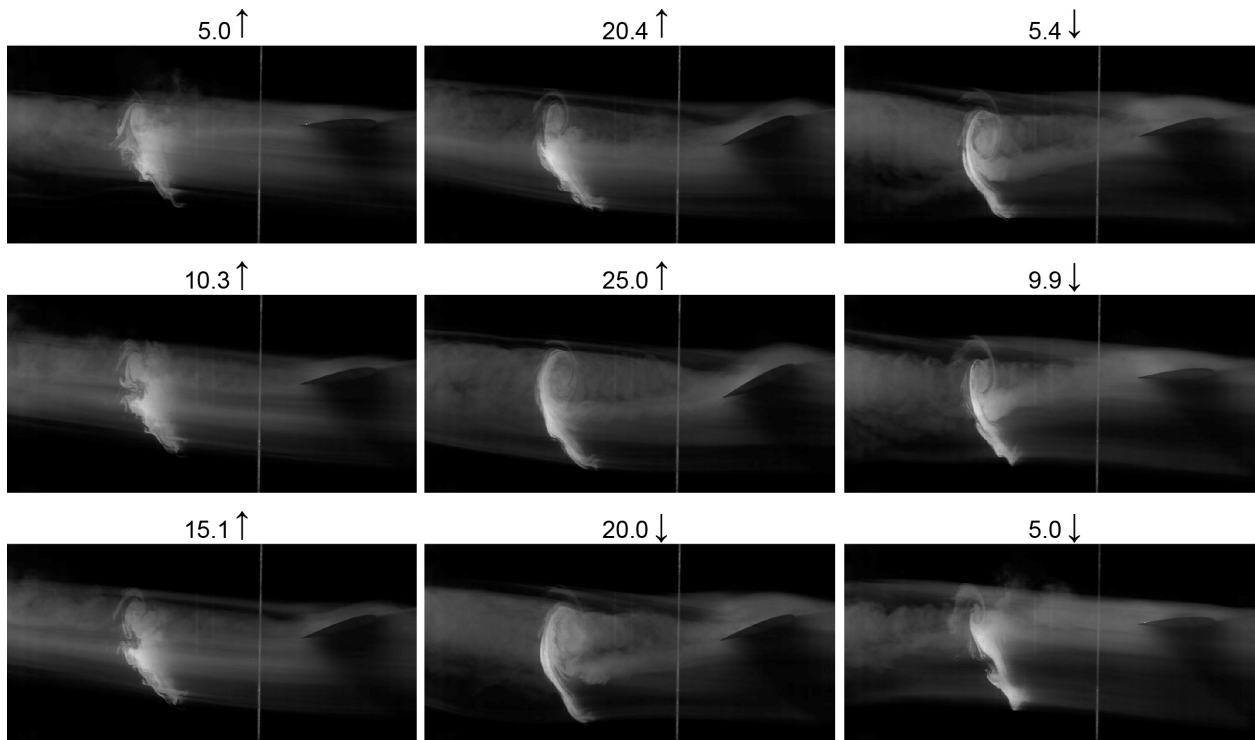
Figure 28.—Winglet shape effect at $x = 3.2$ for $\alpha = 25°$. (a) Rectangular. (b) Triangular. In each column, *U, u', and* ωx are shown in top, middle, and bottom rows, respectively.

Figure 29.—Winglet shape effect at x = 3.2 for α = 25°. (a) Angled out. (b) Angled in. In each column, *U, u′, and* ω_X are shown in top, middle, and bottom rows, respectively.

Figure 30.—Flow visualization pictures with global and laser-sheet illumination for periodically pitched airfoil, $k = 0.2$ ($f = 6.5$ Hz) and $\alpha = 15° \pm 10°$. Laser sheet at $x \approx 3.2$. Approximate α indicated for each picture. Down arrow denotes downward motion of trailing edge (α increasing) and vice versa.
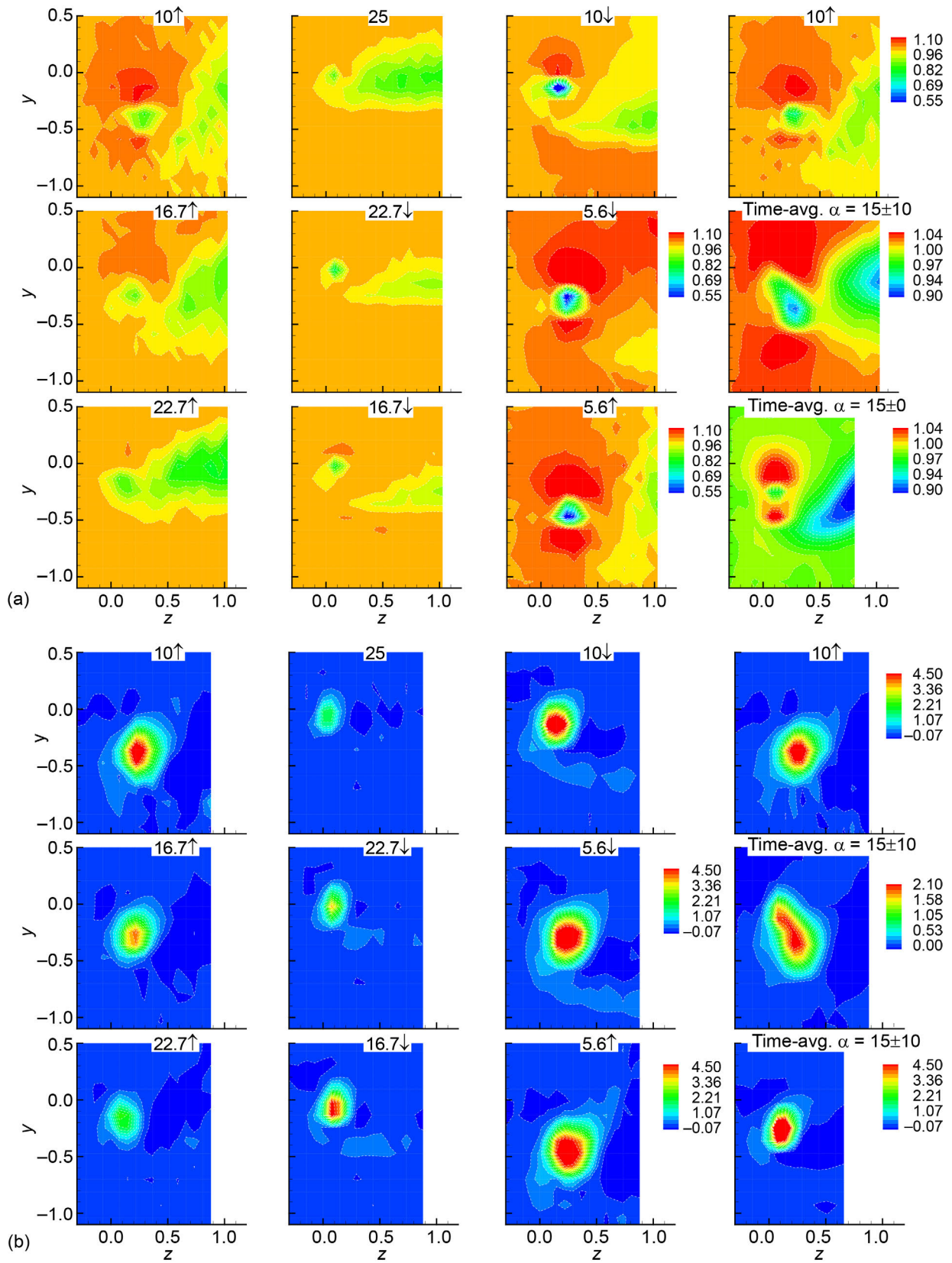
Figure 31.—Phase-averaged data at x = 3.2 for α = 15° ± 10°, k = 0.08. (a) Streamwise velocity <U>. (b) Streamwise vorticity <ω_x>. Corresponding time-averaged data are shown in the right column.

Figure 32.—Phase-averaged data at x = 3.2 for α = 15° ± 10° and k = 0.20. (a) Streamwise velocity <U>. (b) Streamwise vorticity <ω_x>. Corresponding time-averaged data are shown in the right column.
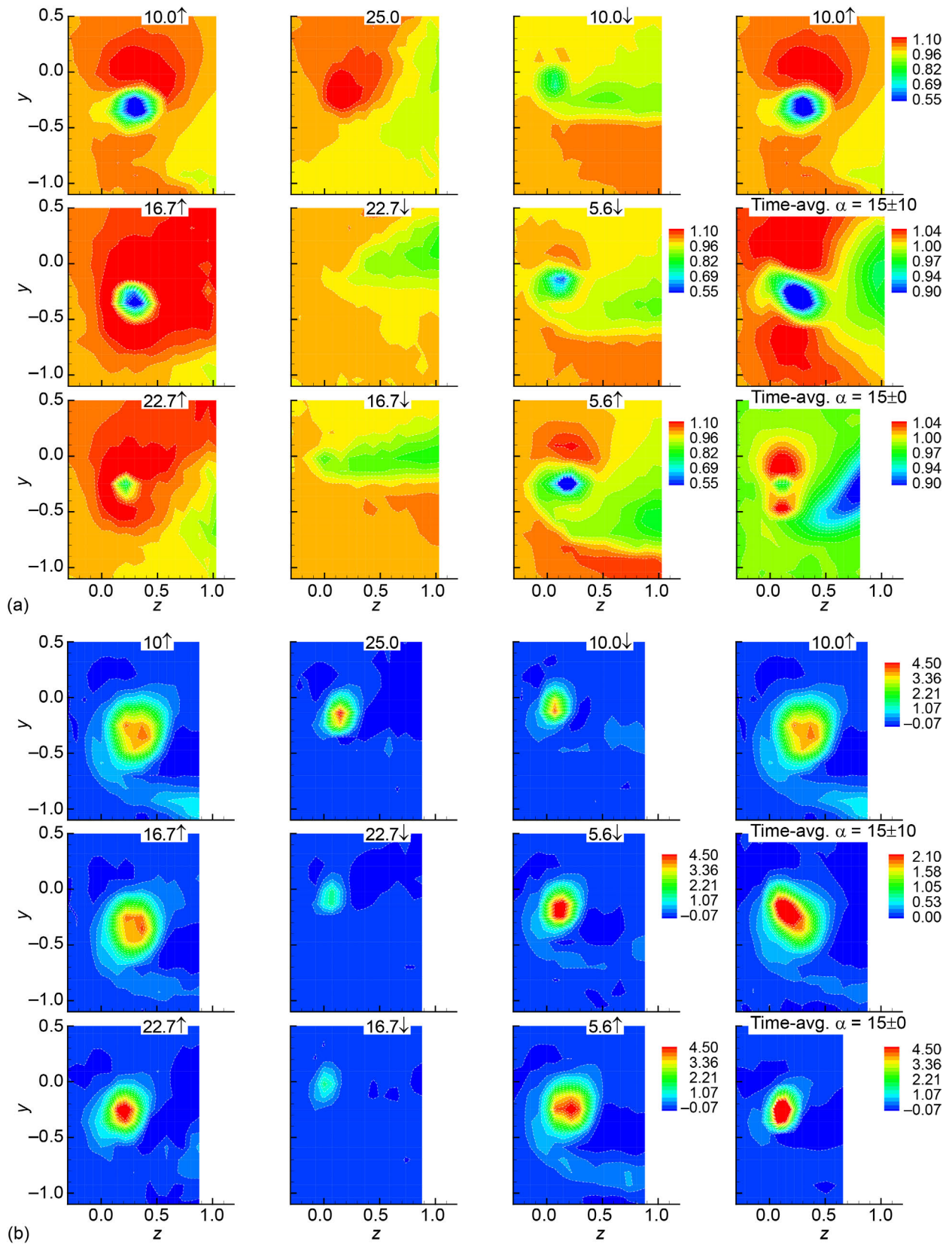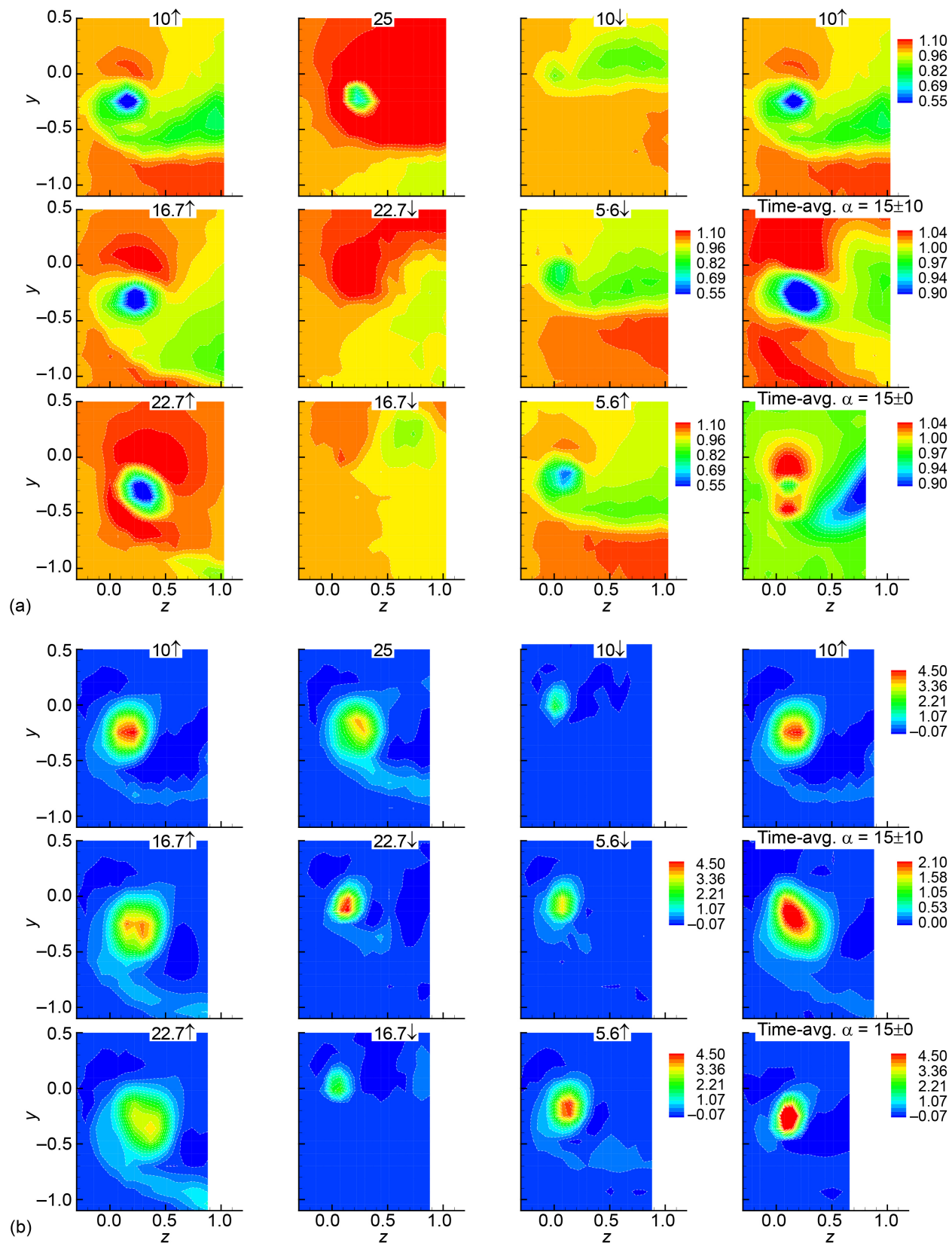
Figure 33.—Phase-averaged data at $x = 3.2$ for $\alpha = 15° \pm 10°$ and $k = 0.33$. (a) Streamwise velocity $<U>$. (b) Streamwise vorticity $<\omega x>$. Corresponding time-averaged data are shown in the right column.

Figure 34.—Phase-averaged data at *x* = 3.2 for α = 15° ± 5° and *k* = 0.20. (a) Streamwise velocity <*U*>. (b) Streamwise vorticity <ω*x*>. Corresponding time-averaged data are shown in the right column.
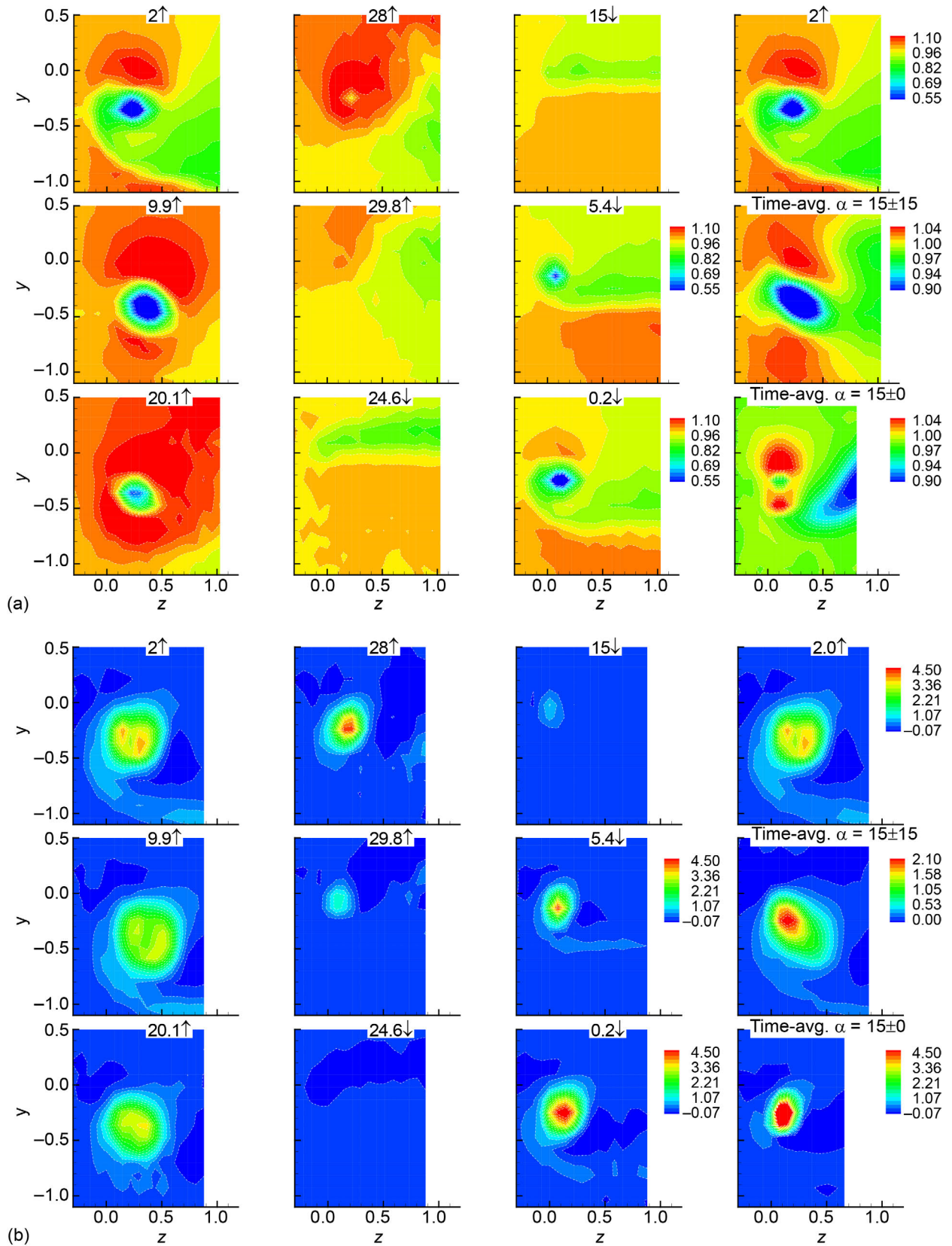
Figure 35.—Phase-averaged data at x = 3.2 for α = 15° ± 15° and k = 0.20. (a) Streamwise velocity $<U>$. (b) Streamwise vorticity $<\omega_x>$. Corresponding time-averaged data are shown in the right column.

Appendix A—Flow Visualization
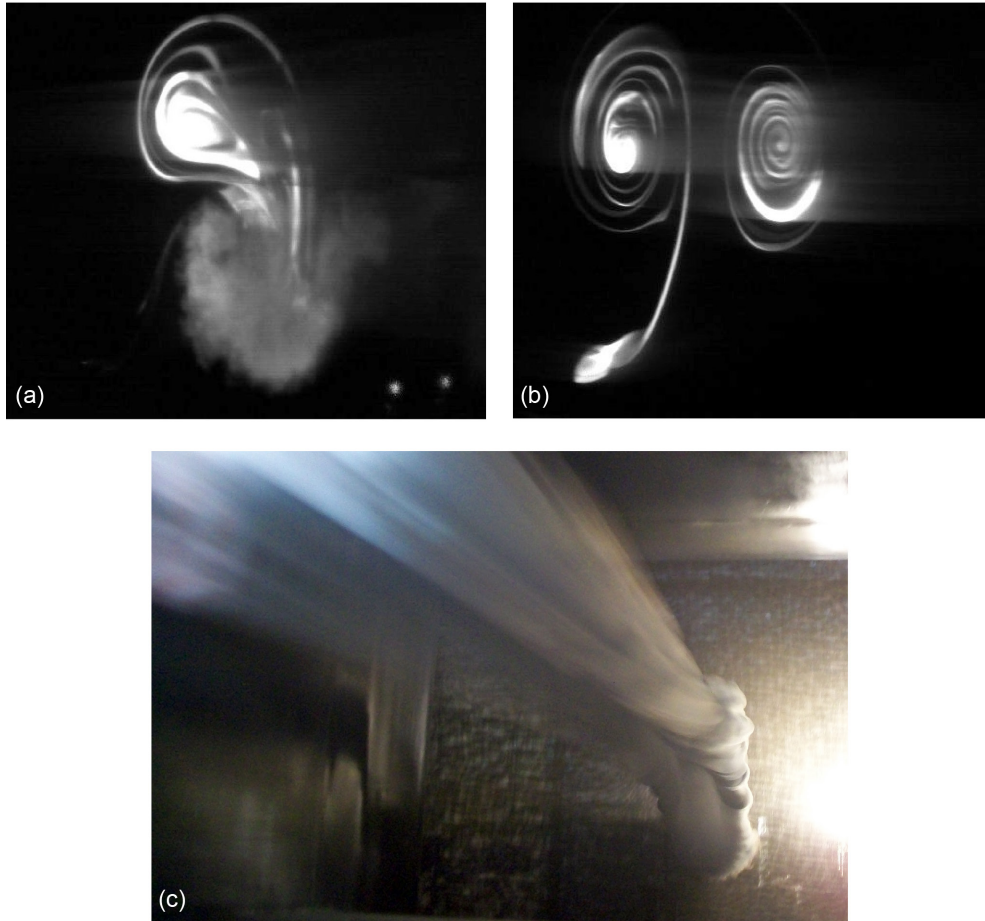

Figure A.1.—Flow visualization attempts with warm smoke (with temperature about 50 °C; ambient temperature about 24 °C). (a) Smoke streak over airfoil tip; α = 35°, U_∞ = 7 m/s, and $x \approx$ 3.2. The laminar-like structure has sense of rotation opposite to that of tip vortex. (b) View corresponding to conditions in (a) but with no airfoil. The "mushroom" structure is due to buoyancy effect accentuated by contraction in the inlet. Left half of mushroom is seen in (a) while right half interacts and merges with tip vortex. (c) Looking upstream, view of smoke streaks within inlet section; $U_\infty \approx$ 5 m/s. Here, smoke is seen emerging through the last screen. Buoyancy effect produces counterrotating vortex pair. (b) Represents a cross section of such a vortex pair.

Appendixes B to E—Supplemental Data

Data are available on a supplemental CD.

References

1. Dreyer, M., et al.: Mind the Gap-Tip Leakage Vortex in Axial Turbines. *IOP Conf. Series: Earth Environ. Sci.*, vol. 22, 2014.
2. Zhou, Chao; and Hodson, Howard: The Tip Leakage Flow of an Unshrouded High Pressure Turbine Blade With Tip Cooling. *J. Turbomach.*, vol. 133, no. 4, 2011.
3. Ameri, A.A.; Steinthorsson, E.; and Rigby, D.L.: Effects of Tip Clearance and Casing Recess on Heat Transfer and Stage Efficiency in Axial Turbines. *J. Turbomach.*, vol. 121, no. 4, 1999, pp. 683−693.
4. Casalino, D.; Hazir, A.; Fares, E.; Duda, B.; and Khorrami, M.R.: On the Connection Between Flap Side-Edge Noise and Tip Vortex Dynamic. *21st AIAA/CEAS Aeroacoustics Conference*, *AIAA Paper* 2015−2992, 2015.
5. Spalart, Philippe R.: Airplane Trailing Vortices. *Ann. Rev. Fluid Mech.*, vol. 30, 1998, pp. 107−138.
6. Margaris, P.; and Gursul, I.: Wing Tip Vortex Control Using Synthetic Jets. *Aeronaut. J.*, vol. 110, no. 1112, 2006, pp. 673−681.
7. Margaris, P.; and Gursul, I.: Vortex Topology of Wing Tip Blowing. *Aerosp. Sci. Technol.*, vol. 14, no. 3, 2010, pp. 143–160.
8. Anik, E.; Abdulrahim, A.; Ostovan, Y.; Mercan, B.; and Uzol, O.: Active Control of Tip Vortex: An Experimental Investigation on the Performance Characteristics of a Model Turbine. *J. Phys.: Conf. Ser.*, vol. 524, 2014.
9. Corsiglia, V.R.; Schwind, R.G.; and Chigier, N.A.: Rapid Scanning, Three-Dimensional Hot-Wire Anemometer Surveys of Wing-Tip Vortices. *J. Aircraft*, vol. 10, no. 12, 1973, pp. 752−757.
10. Orloff, Kenneth L.: Trailing Vortex Wind-Tunnel Diagnostics With a Laser Velocimeter. *J. Aircraft*, vol. 11, no. 8, 1974, pp. 477−482.
11. Devenport, W.J.; Rife, M.C.; Liapis, S.I.; and Follin, G.J.: The Structure and Development of a Wing-Tip Vortex. *J. Fluid Mech.*, vol. 312, 1996, pp. 67−106.
12. Chow, Jim S.; Zilliac, Gregory G.; and Bradshaw, Peter: Mean and Turbulence Measurements in the Near Field of a Wingtip Vortex. *AIAA J.*, vol. 35, no. 10, 1997, pp. 1561−1567.
13. Ramaprian, B.R.; and Zheng, Youxin: Measurement in Rollup Region of the Tip Vortex From a Rectangular Wing. *AIAA J.*, vol. 35, no. 12, 1997, pp. 1837−1843.
14. Anderson, Elgin A.; and Lawton, Todd A.: Correlation Between Vortex Strength and Axial Velocity in a Trailing Vortex. *J. Aircraft*, vol. 40, no. 4, 2003, pp. 699−704.
15. Birch, D.; Lee, T.; Mokhtarian, F.; and Kafyeke, F.: Structure and Induced Drag of a Tip Vortex. *J. Aircraft*, vol. 41, no. 5, 2004, pp. 1138−1145.
16. Lee, T.; and Pereira, J.: Nature of Wakelike and Jetlike Axial Tip Vortex Flows. J. Aircraft, vol. 47, no. 6, 2010, pp. 1946−1954.
17. Ivanell, S.; Leweke, T.; Sarmast, S.; Quaranta, H.U.; Mikkelsen, R.F.; and Sorensen, J.N.: Comparison Between Experiments and Large-Eddy Simulations of Tip Spiral Structure and Geometry. *J. Phys.*: *Conf. Ser.*, vol. 625, 2015, p. 012018.
18. Ramaprian, B.R.; and Zheng, Youxin: Near Field of the Tip Vortex Behind an Oscillating Rectangular Wing. *AIAA J.*, vol. 36, no. 7, 1998, pp. 1263−1269.
19. Birch, D.; and Lee, T.: Investigation of the Near-Field Tip Vortex Behind an Oscillating Wing. *J. Fluid Mech.*, vol. 544, 2005, pp. 201−241.
20. Zaman, K.B.M.Q.; Fagan, A.F.; and Mankbadi, M.R.: Experimental Study of Tip Vortex Flow From a Periodically Pitched Airfoil Section. *AIAA Paper* 2016–1846, 54th AIAA Aerospace Sciences Meeting, San Diego, CA, January 5–8, 2016.
21. Panda, J.; and Zaman, K.B.M.Q.: Experimental Investigation of the Flow Field of an Oscillating Airfoil and Estimation of Lift From Wake Surveys. *J. Fluid Mech.*, vol. 265, 1994, pp. 65−95.
22. Giuni, Michea; and Green, Richard B.: Vortex Formation on Squared and Rounded Tip. *Aerosp. Sci. Technol.*, vol. 29, no. 1, 2013, pp. 191−199.
23. Green, S.I.; and Acosta, A.J.: Unsteady Fow in Trailing Vortices. *J. Fluid Mech.*, vol. 227, 1991, pp. 107−134.

24. Igarashi, H.; Durbin, P.A.; Ma, H.; and Hu, H..: A Stereoscopic PIV Study of a Near-Field Wingtip Vortex. *AIAA Paper* 2010–1029, 48th Aerospace Sciences Meeting, Orlando, FL, 4–7 January, 2010.

25. Chigier, N.A.; and Corsiglia, V.R.: Tip Vortices: Velocity Distributions. NASA TM−X−62087, 1971. http://ntrs.nasa.gov

26. Foss, Judith K.; and Zaman, K.B.M.Q.: Large and Small Scale Vortical Motions in a Shear Layer Perturbed by Tabs. *J. Fluid Mech.*, vol. 382, 1999, pp. 307−329.

27. Gregory, N.; and O'Reilly, C.L.: Low-Speed Aerodynamic Characteristics of NACA 0012 Aerofoil Section, Including the Effects of Upper-Surface Roughness Simulating Hoar Frost. Aeronautical Research Council Reports and Memoranda No. 3726, 1973.

28. Kim, Dong-Ha; Chang, Jo-Won; and Chung, Joon: Low-Reynolds-Number Effect on Aerodynamic Characteristics of a NACA 0012 Airfoil. *J. Aircraft*, vol. 48, no. 4, 2011, pp. 1212−1215.

29. McAlister, K.W.; and Takahashi, R.K.: NACA 0015 Wing Pressure and Trailing Vortex Measurements. NASA TP−3151, 1991. http://ntrs.nasa.gov

30. Gerontakos, P.; and Lee, T.: Effect of Winglet Dihedral on a Tip Vortex. *J. Aircraft*, vol. 43, no. 1, 2006, pp. 117−124.

31. Garmann, Daniel J.; and Visbal, Miguel R.: Analysis of Tip Vortex Near-Wake Evolution for Stationary and Oscillating Wings. *AIAA J.*, vol. 55, no. 8, 2017, pp. 2686−2702.